

MIT Open Access Articles

*Measurement of semi-inclusive $\pi(+)$
electroproduction off the proton*

The MIT Faculty has made this article openly available. **Please share**
how this access benefits you. Your story matters.

Citation: Osipenko, M. et al. "Measurement of Semi-inclusive π^+ Electroproduction Off the Proton." Physical Review D 80.3 (2009) : n. pag. © 2009 The American Physical Society

As Published: <http://dx.doi.org/10.1103/PhysRevD.80.032004>

Publisher: American Physical Society

Persistent URL: <http://hdl.handle.net/1721.1/65096>

Version: Final published version: final published article, as it appeared in a journal, conference proceedings, or other formally published context

Terms of Use: Article is made available in accordance with the publisher's policy and may be subject to US copyright law. Please refer to the publisher's site for terms of use.



Measurement of semi-inclusive π^+ electroproduction off the proton

M. Osipenko,^{16,23} M. Ripani,¹⁶ G. Ricco,¹⁶ H. Avakian,³¹ R. De Vita,¹⁶ G. Adams,²⁸ M. J. Amarian,²⁷ P. Ambrozewicz,¹¹ M. Anghinolfi,¹⁶ G. Asryan,⁴⁵ H. Bagdasaryan,^{45,27} N. Baillie,⁸ J. P. Ball,² N. A. Baltzell,⁴² S. Barrow,¹² M. Battaglieri,¹⁶ I. Bedlinskiy,¹⁸ M. Bektasoglu,^{27,*} M. Bellis,^{28,4} N. Benmouna,³⁰ B. L. Berman,³⁰ A. S. Biselli,^{28,10} L. Blaszczyk,¹² B. E. Bonner,²⁹ S. Bouchigny,¹⁷ S. Boiarinov,^{18,31} R. Bradford,⁴ D. Branford,⁹ W. J. Briscoe,³⁰ W. K. Brooks,^{33,31} S. Bültmann,²⁷ V. D. Burkert,³¹ C. Butuceanu,⁸ J. R. Calarco,³⁹ S. L. Careccia,²⁷ D. S. Carman,³¹ A. Cazes,⁴² F. Ceccopieri,^{34,14} S. Chen,¹² P. L. Cole,^{31,13} P. Collins,² P. Coltharp,¹² P. Corvisiero,¹⁶ D. Crabb,⁴³ V. Crede,¹² J. P. Cummings,²⁸ N. Dashyan,⁴⁵ R. De Masi,⁶ E. De Sanctis,¹⁵ P. V. Degtyarenko,³¹ H. Denizli,⁴⁰ L. Dennis,¹² A. Deur,³¹ K. V. Dharmawardane,²⁷ K. S. Dhuga,³⁰ R. Dickson,⁴ C. Djalali,⁴² G. E. Dodge,²⁷ J. Donnelly,³⁷ D. Doughty,^{7,31} V. Drozdov,^{23,16} M. Dugger,² S. Dytman,⁴⁰ O. P. Dzyubak,⁴² H. Egiyan,^{8,31,†} K. S. Egiyan,^{45,‡} L. El Fassi,¹ L. Elouadrhiri,³¹ P. Eugenio,¹² R. Fatemi,⁴³ G. Fedotov,²³ G. Feldman,³⁰ R. J. Feuerbach,⁴ H. Funsten,^{8,4} M. Garçon,⁶ G. Gavalian,^{39,27} G. P. Gilfoyle,⁴¹ K. L. Giovanetti,²⁰ F. X. Girod,⁶ J. T. Goetz,³⁵ E. Golovach,²³ A. Gonenc,¹¹ C. I. O. Gordon,³⁷ R. W. Gothe,⁴² K. A. Griffioen,⁸ M. Guidal,¹⁷ M. Guillo,⁴² N. Guler,²⁷ L. Guo,³¹ V. Gyurjyan,³¹ C. Hadjidakis,¹⁷ K. Hafidi,¹ H. Hakobyan,⁴⁵ R. S. Hakobyan,⁵ C. Hanretty,¹² J. Hardie,^{7,31} N. Hassall,³⁷ D. Heddle,³¹ F. W. Hersman,³⁹ K. Hicks,²⁶ I. Hleiqawi,²⁶ M. Holtrop,³⁹ C. E. Hyde-Wright,²⁷ Y. Ilieva,³⁰ A. Ilyichev,²⁴ D. G. Ireland,³⁷ B. S. Ishkhanov,²³ E. L. Isupov,²³ M. M. Ito,³¹ D. Jenkins,⁴⁴ H. S. Jo,¹⁷ K. Joo,^{31,36} H. G. Juengst,²⁷ N. Kalantarians,²⁷ J. D. Kellie,³⁷ M. Khandaker,²⁵ W. Kim,²¹ A. Klein,²⁷ F. J. Klein,⁵ A. V. Klimenko,²⁷ M. Kossov,¹⁸ Z. Krahn,⁴ L. H. Kramer,^{11,31} V. Kubarovskiy,²⁸ J. Kuhn,^{28,4} S. E. Kuhn,²⁷ S. V. Kuleshov,³³ J. Lachniet,^{4,27} J. M. Laget,^{6,31} J. Langheinrich,⁴² D. Lawrence,³⁸ Ji Li,²⁸ K. Livingston,³⁷ H. Y. Lu,⁴² M. MacCormick,¹⁷ N. Markov,³⁶ P. Mattione,²⁹ S. McAleer,¹² M. McCracken,⁴ B. McKinnon,³⁷ J. W. C. McNabb,⁴ B. A. Mecking,³¹ S. Mehrabyan,⁴⁰ J. J. Melone,³⁷ M. D. Mestayer,³¹ C. A. Meyer,⁴ T. Mibe,²⁶ K. Mikhailov,¹⁸ R. Minehart,⁴³ M. Mirazita,¹⁵ R. Miskimen,³⁸ V. Mokeev,^{23,31} K. Moriya,⁴ S. A. Morrow,^{17,6} M. Moteabbed,¹¹ J. Mueller,⁴⁰ E. Munevar,³⁰ G. S. Mutchler,^{29,‡} P. Nadel-Turonski,³⁰ J. Napolitano,²⁸ R. Nasseripour,^{11,42} S. Niccolai,^{30,17} G. Niculescu,^{26,20} I. Niculescu,^{30,31,20} B. B. Niczyporuk,³¹ M. R. Niroula,²⁷ R. A. Niyazov,^{28,31} M. Nozar,³¹ G. V. O’Rielly,³⁰ A. I. Ostrovidov,¹² K. Park,²¹ E. Pasyuk,² C. Paterson,³⁷ S. Anefalos Pereira,¹⁵ S. A. Philips,³⁰ J. Pierce,⁴³ N. Pivnyuk,¹⁸ D. Pocanic,⁴³ O. Pogorelko,¹⁸ E. Polli,¹⁵ I. Popa,³⁰ S. Pozdniakov,¹⁸ B. M. Freedom,⁴² J. W. Price,³ Y. Prok,^{43,§} D. Protopopescu,^{39,37} L. M. Qin,²⁷ B. A. Raue,^{11,31} G. Riccardi,¹² B. G. Ritchie,² G. Rosner,³⁷ P. Rossi,¹⁵ P. D. Rubin,⁴¹ F. Sabatié,⁶ J. Salamanca,¹³ C. Salgado,²⁵ J. P. Santoro,^{44,31,||} V. Sapunenko,³¹ R. A. Schumacher,⁴ V. S. Serov,¹⁸ Y. G. Sharabian,³¹ N. V. Shvedunov,²³ A. V. Skabelin,²² E. S. Smith,³¹ L. C. Smith,⁴³ D. I. Sober,⁵ D. Sokhan,⁹ A. Stavinsky,¹⁸ S. S. Stepanyan,²¹ S. Stepanyan,³¹ B. E. Stokes,¹² P. Stoler,²⁸ I. I. Strakovsky,³⁰ S. Strauch,^{30,42} M. Taiuti,¹⁶ D. J. Tedeschi,⁴² U. Thoma,^{31,19,¶} A. Tkabladze,^{30,*} S. Tkachenko,²⁷ L. Todor,^{4,**} L. Trentadue,^{34,14} C. Tur,⁴² M. Ungaro,^{28,36} M. F. Vineyard,^{32,41} A. V. Vlassov,¹⁸ D. P. Watts,^{37,††} L. B. Weinstein,²⁷ D. P. Weygand,³¹ M. Williams,⁴ E. Wolin,³¹ M. H. Wood,^{42,‡‡} A. Yegneswaran,³¹ L. Zana,³⁹ J. Zhang,²⁷ B. Zhao,³⁶ and Z. W. Zhao⁴²

(CLAS Collaboration)

¹Argonne National Laboratory, Argonne, Illinois 60439²Arizona State University, Tempe, Arizona 85287-1504³California State University, Dominguez Hills, Carson, California 90747⁴Carnegie Mellon University, Pittsburgh, Pennsylvania 15213⁵Catholic University of America, Washington, D.C. 20064⁶CEA-Saclay, Service de Physique Nucléaire, 91191 Gif-sur-Yvette, France⁷Christopher Newport University, Newport News, Virginia 23606⁸College of William and Mary, Williamsburg, Virginia 23187-8795⁹Edinburgh University, Edinburgh EH9 3JZ, United Kingdom¹⁰Fairfield University, Fairfield Connecticut 06824¹¹Florida International University, Miami, Florida 33199¹²Florida State University, Tallahassee, Florida 32306¹³Idaho State University, Pocatello, Idaho 83209¹⁴INFN, Gruppo Collegato di Parma, 43100 Parma, Italy¹⁵INFN, Laboratori Nazionali di Frascati, 00044 Frascati, Italy¹⁶INFN, Sezione di Genova, 16146 Genova, Italy¹⁷Institut de Physique Nucleaire ORSAY, Orsay, France

- ¹⁸*Institute of Theoretical and Experimental Physics, Moscow, 117259, Russia*
¹⁹*Institute für Strahlen und Kernphysik, Universität Bonn, Germany 53115*
²⁰*James Madison University, Harrisonburg, Virginia 22807*
²¹*Kyungpook National University, Daegu 702-701, South Korea*
²²*Massachusetts Institute of Technology, Cambridge, Massachusetts 02139-4307*
²³*Moscow State University, Skobeltsyn Institute of Nuclear Physics, 119899 Moscow, Russia*
²⁴*National Scientific and Educational Centre of Particle and High Energy, Physics of the Belarusian State University, 220040 Minsk, Belarus*
²⁵*Norfolk State University, Norfolk, Virginia 23504*
²⁶*Ohio University, Athens, Ohio 45701*
²⁷*Old Dominion University, Norfolk, Virginia 23529*
²⁸*Rensselaer Polytechnic Institute, Troy, New York 12180-3590*
²⁹*Rice University, Houston, Texas 77005-1892*
³⁰*The George Washington University, Washington, D.C. 20052*
³¹*Thomas Jefferson National Accelerator Facility, Newport News, Virginia 23606*
³²*Union College, Schenectady, New York 12308*
³³*Universidad Técnica Federico Santa María, Av. España 1680, Casilla 110-V Valparaíso, Chile*
³⁴*Università di Parma, 43100 Parma, Italy*
³⁵*University of California at Los Angeles, Los Angeles, California 90095-1547*
³⁶*University of Connecticut, Storrs, Connecticut 06269*
³⁷*University of Glasgow, Glasgow G12 8QQ, United Kingdom*
³⁸*University of Massachusetts, Amherst, Massachusetts 01003*
³⁹*University of New Hampshire, Durham, New Hampshire 03824-3568*
⁴⁰*University of Pittsburgh, Pittsburgh, Pennsylvania 15260*
⁴¹*University of Richmond, Richmond, Virginia 23173*
⁴²*University of South Carolina, Columbia, South Carolina 29208*
⁴³*University of Virginia, Charlottesville, Virginia 22901*
⁴⁴*Virginia Polytechnic Institute and State University, Blacksburg, Virginia 24061-0435*
⁴⁵*Yerevan Physics Institute, 375036 Yerevan, Armenia*
- (Received 6 September 2008; published 21 August 2009)

Semi-inclusive π^+ electroproduction on protons has been measured with the CLAS detector at Jefferson Lab. The measurement was performed on a liquid-hydrogen target using a 5.75 GeV electron beam. The complete five-fold differential cross sections were measured over a wide kinematic range including the complete range of azimuthal angles between hadronic and leptonic planes, ϕ , enabling us to separate the ϕ -dependent terms. Our measurements of the ϕ -independent term of the cross section at low Bjorken x were found to be in fairly good agreement with pQCD calculations. Indeed, the conventional current fragmentation calculation can account for almost all of the observed cross section, even at small π^+ momentum. The measured center-of-momentum spectra are in qualitative agreement with high-energy data, which suggests a surprising numerical similarity between the spectator diquark fragmentation in the present reaction and the antiquark fragmentation measured in e^+e^- collisions. We have observed that the two ϕ -dependent terms of the cross section are small. Within our precision the $\cos 2\phi$ term is compatible with zero, except for the low- z region, and the measured $\cos\phi$ term is much smaller in magnitude than the sum of the Cahn and Berger effects.

DOI: 10.1103/PhysRevD.80.032004

PACS numbers: 13.60.Le, 12.38.Bx, 12.38.Qk

I. INTRODUCTION

The semi-inclusive lepton production of hadrons off the nucleon, $eN \rightarrow e'hX$, is an important tool allowing to

study simultaneously the internal structure of the target nucleon and hadron creation mechanism. In the deep inelastic scattering (DIS) regime the semi-inclusive lepton production of hadrons can be described by perturbative

*Current address: Ohio University, Athens, Ohio 45701

†Current address: University of New Hampshire, Durham, New Hampshire 03824-3568

‡Deceased

§Current address: Massachusetts Institute of Technology, Cambridge, Massachusetts 02139-4307

¶Current address: Catholic University of America, Washington, D.C. 20064

¶¶Current address: Physikalisches Institut der Universität Giessen, 35392 Giessen, Germany

**Current address: University of Richmond, Richmond, Virginia 23173

††Current address: Edinburgh University, Edinburgh EH9 3JZ, United Kingdom

‡‡Current address: University of Massachusetts, Amherst, Massachusetts 01003

quantum chromodynamics (pQCD) combining nonperturbative distribution/fragmentation functions. Semi-inclusive leptonproduction of hadrons in DIS (SIDIS) can occur through current or target fragmentation [1] (see Fig. 1). Current fragmentation is the hadronization of the struck quark, while target fragmentation is hadronization of the spectator. Both nonperturbative, soft fragmentation mechanisms factorize from the hard virtual-photon/parton scattering amplitude in pQCD (see Ref. [2] for the current fragmentation and Refs. [3,4] for the target fragmentation).

Inclusive lepton scattering off the nucleon and hadron production in e^+e^- collisions allow one to study separately the fractional momentum dependence of the parton distribution functions for the nucleon and the parton fragmentation functions, respectively. The leptonproduction of hadrons in the current fragmentation region combines these two and provides additional information about hadronization and nucleon structure. In fact, for DIS, semi-inclusive measurements provide new information about the transverse momentum distribution (TMD) of partons, which is important for understanding the role of orbital angular momenta of quarks and gluons [5]. Furthermore, the detection of a hadron in SIDIS introduces a flavor selectivity for the observed parton distributions. In contrast, target fragmentation is described by fracture functions, present only in the semi-inclusive reactions.

The finite transverse momentum of partons in the initial state leads to an azimuthal variation in the cross section, as does the transverse spin of partons in the unpolarized nucleon.

In order to achieve the SIDIS regime sufficiently high beam energy is mandatory. By decreasing the beam energy higher order (in pQCD) and higher twist effects appear, spoiling the agreement between the experimental data and

theoretical pQCD expectations. Therefore, only a comparison between the actual data and theoretical calculations can reveal the dominance of SIDIS dynamics in the experiment. Though, a good agreement between data and theory in one observable does not necessarily guarantee SIDIS dominance in others.

Previous measurements [6–10] have verified these factorizations experimentally and have tested pQCD predictions. Measurements of unpolarized semi-inclusive lepton-nucleon scattering have been performed at several facilities such as CERN (EMC [6]), Fermilab (E655 [7]), DESY (H1 [8], ZEUS [9], HERMES [10]), SLAC [11], Cornell [12–14] and Jefferson Lab (Hall C) [15,16]. The last two experiments covered a kinematical region similar to the present measurement. Despite all of these measurements, open questions remain about the target fragmentation mechanism and the physics behind the azimuthal distributions. The measurements at high beam energies (EMC, E655, H1 and ZEUS) covered a broad kinematic range, but lacked particle identification and the statistics to look at differential cross sections in more than two kinematic variables (the latter applies also to HERMES). Experiments at lower energies (SLAC, Cornell and Hall C of Jefferson Lab) using classical spectrometers measured cross sections only at a few kinematic points. To improve the current knowledge of semi-inclusive lepton-nucleon scattering one has to combine the broad coverage of high-energy experiments with high luminosity and particle identification in order to measure the fully differential cross section for a specified hadron.

Semi-inclusive hadron electroproduction, $\gamma_\nu(q) + p(P) \rightarrow h(p_h) + X$, is completely described by a set of five kinematic variables. The variables q , P and p_h in parentheses denote four-momenta of the virtual photon γ_ν , the proton p and the observed hadron h . The letter X denotes the unobserved particles in the reaction. In this article we have chosen a commonly used set of independent variables: the virtual-photon four-momentum transfer squared $Q^2 = -q^2 =^{\text{Lab}} 4E_0E'\sin^2\frac{\theta}{2}$, the Bjorken scaling variable $x = -\frac{q^2}{2P \cdot q} =^{\text{Lab}} \frac{Q^2}{2M\nu}$, the virtual-photon energy fraction carried by the hadron $z = \frac{P \cdot p_h}{P \cdot q} =^{\text{Lab}} \frac{E_h}{\nu}$, the squared hadron spatial transverse momentum with respect to the virtual-photon direction p_T^2 and the angle between the leptonic and hadronic planes ϕ [17] (see Fig. 2). Here E_0 is the beam energy, E' and θ are the scattered electron energy and angle, $\nu = E_0 - E'$ is the virtual photon energy in the lab frame, and M is the proton mass. We will also use momentum transfer $t = (q - p_h)^2$, Feynman $x_F = 2p_{\parallel}^{\text{CM}}/W$ and the projection of the hadron momentum onto the photon direction p_{\parallel} as alternative variables when they help with the physical interpretation. Here $W = \sqrt{(q + P)^2}$ is the invariant mass of the final hadronic system and the CM label denotes the center-of-momentum frame.

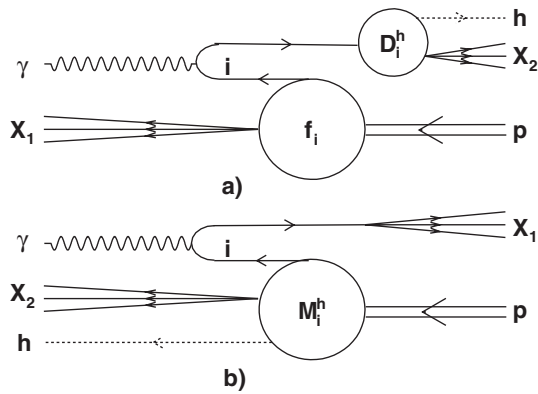


FIG. 1. Schematic representation of current (a) and target (b) fragmentation processes in the virtual photon-proton center-of-momentum frame neglecting transverse momenta of particles. Blobs represent nonperturbative functions: the parton density function $f_i(x)$, parton fragmentation function $D_i^h(z)$ and fracture function $M_i^h(x, z)$ as given in Eq. (29). X_1 and X_2 indicate two components of the undetected final state hadronic system X .

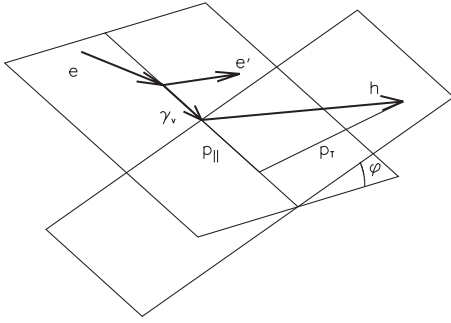


FIG. 2. Definition of the azimuthal angle between the leptonic and hadronic planes ϕ and hadron momentum components p_T and p_{\parallel} .

The CEBAF Large Acceptance Spectrometer (CLAS) in Hall B at Jefferson Lab allows us to study the five-fold differential semi-inclusive cross section over a large range of four-momentum transfer Q^2 from 1.4 to 7 (GeV/c)² and Bjorken x from 0.15 to 1 (see Fig. 3). CLAS enables us to measure distributions of the outgoing meson (z from 0.07 to 1 and p_T^2 from 0.005 to 1.5 (GeV/c)²), in particular, full coverage in the azimuthal distributions that is very important. However, the covered kinematical interval is not rectangular in all five dimensions leading to a shrinkage of the four-dimensional acceptance when one of variables reaches its limits. The CLAS detector also has good parti-

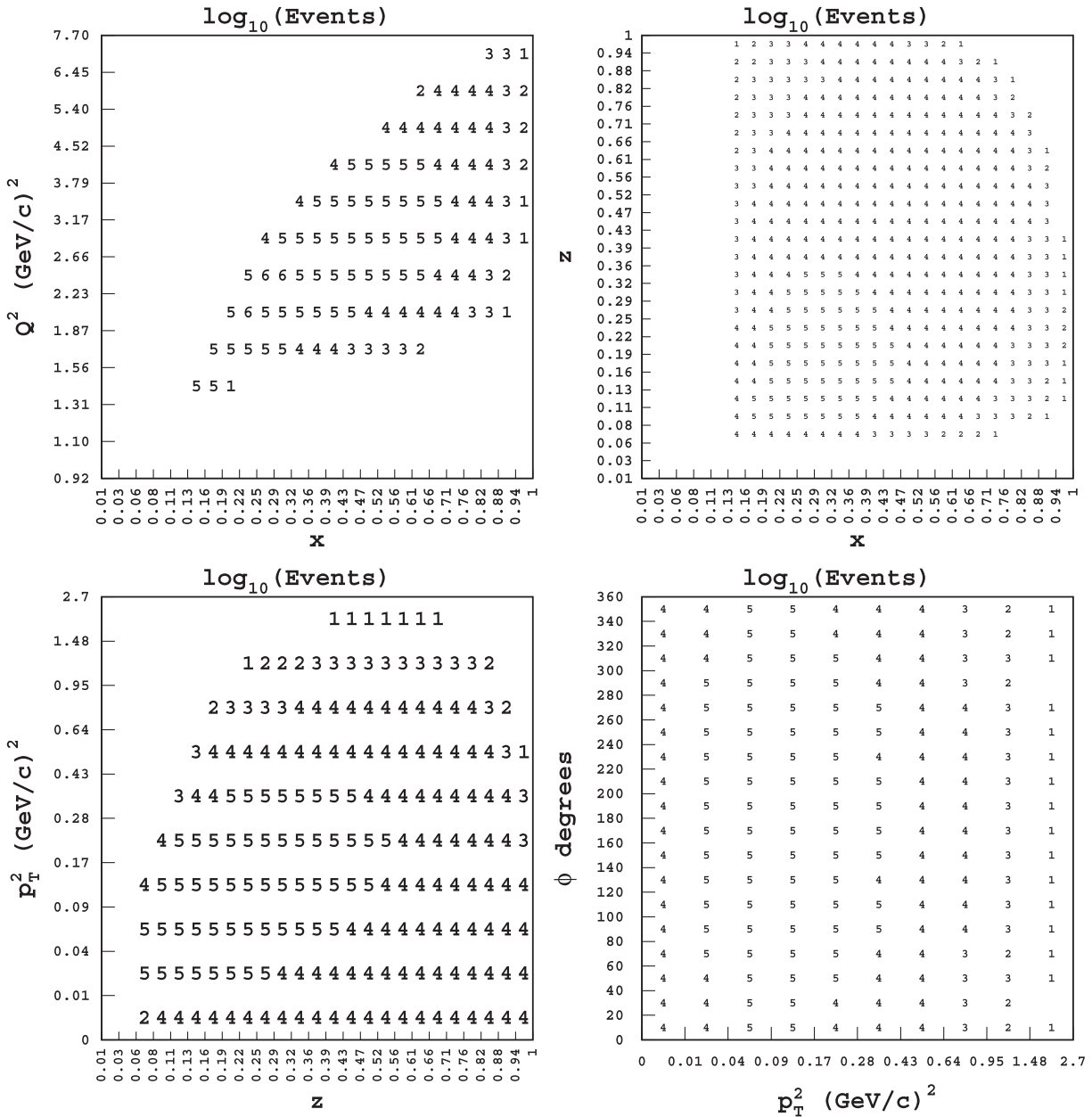


FIG. 3. Kinematical regions covered by the present experiment in different independent variables. Numbers on the plots give base-10 logarithm of the number of events.

cle identification capabilities, resulting in a clean selection of pions for this analysis.

II. FORMALISM AND THEORETICAL EXPECTATIONS

The unpolarized semi-inclusive cross section can be written in terms of four independent Lorentz-invariant structure functions [18]:

$$\frac{d^5\sigma}{dx dQ^2 dz dp_T^2 d\phi} = \frac{2\pi\alpha^2}{xQ^4} \frac{E_h}{|p_{\parallel}|} \zeta \left[\epsilon \mathcal{H}_1 + \mathcal{H}_2 + 2(2-y) \right. \\ \left. \times \sqrt{\frac{\kappa}{\zeta}} \cos\phi \mathcal{H}_3 + 2\kappa \cos 2\phi \mathcal{H}_4 \right], \quad (1)$$

where inelasticity $y = \nu/E_0$, $\gamma = \frac{2Mx}{\sqrt{Q^2}}$, $\zeta = 1 - y - \frac{1}{4}\gamma^2 y^2$, $\epsilon = \frac{xy^2}{\zeta}$, $\kappa = \frac{1}{1+\gamma^2}$ and $\mathcal{H}_i = \mathcal{H}_i(x, z, Q^2, p_T^2)$. In contrast to Ref. [18], we absorbed the $\sqrt{p_T^2/Q^2}$ and p_T^2/Q^2 coefficients in front of the structure functions \mathcal{H}_3 and \mathcal{H}_4 , respectively, into the structure function definition to let \mathcal{H}_4 reflect the recently identified leading twist contribution by Boer and Mulders [19]. Both structure functions include also an additional factor $\frac{1}{2}$ to simplify relation with the azimuthal moments.

In order to disentangle all four structure functions \mathcal{H}_i , one has to measure the complete five-fold differential semi-inclusive cross section at a few different beam energies (as proposed in Ref. [20]). In the present work we have data for only a single beam energy, and we relied upon the separation between the longitudinal ($\sigma_L \sim \mathcal{H}_2/\kappa - 2x\mathcal{H}_1$) and transverse ($\sigma_T \sim 2x\mathcal{H}_1$) cross sections performed in Ref. [21] and found to be compatible with $R = 0.12 \pm 0.06$ (the weighted average over proton and deuteron data):

$$\frac{\mathcal{H}_1}{\mathcal{H}_2} = \frac{1}{2\kappa x} \frac{\sigma_T}{\sigma_T + \sigma_L} = \frac{1}{2\kappa x} \frac{1}{1+R}, \quad (2)$$

where $R = \sigma_L/\sigma_T$ is the longitudinal to transverse cross section ratio.

The azimuthal moments can be expressed in terms of the structure functions \mathcal{H}_i as follows:

$$\langle \cos\phi \rangle = (2-y) \sqrt{\frac{\kappa}{\zeta}} \frac{\mathcal{H}_3}{\mathcal{H}_2 + \epsilon\mathcal{H}_1}, \quad (3) \\ \langle \cos 2\phi \rangle = \kappa \frac{\mathcal{H}_4}{\mathcal{H}_2 + \epsilon\mathcal{H}_1}.$$

These relations allow us to extract azimuthal moments from the data in order to determine \mathcal{H}_3 and \mathcal{H}_4 .

The SIDIS cross section integrated over ϕ and p_T^2 is given by [18,22]:

$$\frac{d^3\sigma}{dx dQ^2 dz} = \frac{4\pi\alpha^2}{xQ^4} \left[xy^2 H_1(x, z, Q^2) \right. \\ \left. + \left(1 - y - \frac{Mxy}{2E_0} \right) H_2(x, z, Q^2) \right], \quad (4)$$

where roman H_i are defined as calligraphic \mathcal{H}_i structure functions integrated over p_T^2 . In the parton model, the initial momentum of the struck quark is given by the proton momentum multiplied by the light-cone fraction x . If we instead consider the momentum carried by the struck quark after absorption of the virtual photon, then z represents the light-cone fraction of the momentum taken away by the produced hadron. In the region of forward-going hadron (frame dependent) this cross section can be evaluated as the convolution of the parton density function $f(x, Q^2)$ obtained in inclusive processes and the parton fragmentation function $D^h(z, Q^2)$ measured in e^+e^- collisions:

$$H_2(x, z, Q^2) = \sum_i e_i^2 x f_i(x, Q^2) \otimes D_i^h(z, Q^2), \quad (5)$$

where the sum runs over quark flavors i and e_i is the charge of i th flavor quark. Instead, in the region of backward-going hadron (frame dependent) the cross section is proportional to the fracture function [1] $M^h(x, z, Q^2)$ uniquely defined in the semi-inclusive processes:

$$H_2(x, z, Q^2) = \sum_i e_i^2 x (1-x) M_i^h(x, z, Q^2). \quad (6)$$

The separation between the two processes is frame dependent and can only be studied phenomenologically.

Values of the parton density function $f(x, Q^2)$ and the parton fragmentation function $D^h(z, Q^2)$ can be obtained in pQCD inspired world data fits, e.g. in Refs. [23–28], respectively, but only Ref. [26] allows for hadron charge separation. The fracture function is only studied for proton and neutron production [29,30] and π^+ fracture function is completely unknown.

In practice the measured cross section also depends on the transverse momentum p_T of the hadron. The intrinsic motion of partons in the proton (Cahn effect [31]) leads to an exponential p_T^2 -behavior of the structure function \mathcal{H}_2 :

$$\mathcal{H}_2(x, z, Q^2, p_T^2) = \frac{H_2(x, Q^2, z)}{\pi \langle p_T^2 \rangle} \exp[-p_T^2/\langle p_T^2 \rangle]. \quad (7)$$

The mean squared transverse momentum in the naive parton model is given by the sum of two terms [32–34]:

$$\langle p_T^2 \rangle = b^2 + a^2 z^2, \quad (8)$$

where a^2 is the mean squared intrinsic transverse momentum of the partons, $a^2 z^2$ is the mean squared parton transverse momentum transferred to the hadron, and b^2 is the mean squared transverse momentum acquired during fragmentation.

The ϕ -dependent terms in Eq. (1) also appear in next-to-leading-order (NLO) pQCD because the radiation of hard

gluons leads to an azimuthal variation [22]. However, this effect is expected to be important at energies higher than that of the present experiment [34]. This is because the transverse momentum generated by the hard gluon is generally larger than that accessible in our experiment. In our energy range, the main contributions to the ϕ -dependence of the cross sections are expected to be the Cahn and Berger [35] effects for \mathcal{H}_3 and the Boer-Mulders function [19] for \mathcal{H}_4 (see also Refs. [36–39]). The Cahn effect arises from the simple kinematics of partons with transverse momentum and can be calculated explicitly in the limits $Q^2 \rightarrow \infty$ and $z \rightarrow 1$ (see Refs. [32–34,40]).

The Berger effect is the exclusive production of a single pion from a free, struck quark that radiates a gluon, produces a $q\bar{q}$ pair, and recombines with the \bar{q} . The formation of this pion through one-gluon exchange yields a $\cos\phi$ dependence proportional to the hadron wave function. Since such a production mechanism does not require any initial transverse momentum of a struck parton it is completely orthogonal to the Cahn effect.

Explicitly neglecting intrinsic parton transverse momentum one has [41]:

$$\frac{\mathcal{H}_3}{\mathcal{H}_2 + \epsilon\mathcal{H}_1} = \frac{zI_1(I_2 - \frac{p_T^2}{Q^2}I_1)}{\eta I_2^2 + (4z^2 + \eta \frac{p_T^2}{Q^2}) \frac{p_T^2}{Q^2} I_1^2} \sqrt{\frac{p_T^2}{Q^2}} \quad (9)$$

and

$$\frac{\mathcal{H}_4}{\mathcal{H}_2 + \epsilon\mathcal{H}_1} = - \frac{I_1 I_2}{\eta I_2^2 + (4z^2 + \eta \frac{p_T^2}{Q^2}) \frac{p_T^2}{Q^2} I_1^2} \frac{p_T^2}{Q^2}. \quad (10)$$

Here we defined

$$I_1 = z \int_0^1 d\xi \frac{\psi(\xi)}{z - \xi(z^2 - \frac{p_T^2}{Q^2})} \quad (11)$$

and

$$I_2 = \int_0^1 d\xi \frac{\psi(\xi)}{1 - \xi} - z^2 I_1, \quad (12)$$

with $\psi(\xi)$ being the pion wave function and $\eta = 1 + \epsilon/2x$.

The contribution of the Boer-Mulders function gives the probability to find a transversely polarized quark in the unpolarized proton. Explicitly in leading-order (LO) pQCD and $p_T^2/Q^2 \rightarrow 0$ one has [19]:

$$\begin{aligned} \frac{\mathcal{H}_4}{\mathcal{H}_2 + \epsilon\mathcal{H}_1} &= \frac{1-y}{1+(1-y)^2} \frac{p_T^2}{M m_h} \frac{8}{\kappa} \\ &\times \frac{\sum_i e_i^2 x h_i^\perp(x) H_i^{\perp h}(z)}{\sum_i e_i^2 x f_i(x) D_i^h(z)}, \end{aligned} \quad (13)$$

where m_h is the mass of the detected hadron, $h_i^\perp(x)$ is the momentum distribution of transversely polarized quarks in

the unpolarized proton (Boer-Mulders function) and $H_i^{\perp h}(z)$ is the Collins fragmentation function [42] describing fragmentation of a transversely polarized quark into a polarized hadron. The Collins fragmentation function was parametrized using e^+e^- data in Ref. [43].

These three main effects predict different kinematic dependencies. For example, the contribution of the Boer-Mulders function in \mathcal{H}_4 is of leading order, and therefore should scale with Q^2 . On the other hand, both the Cahn and Berger effects have a nonperturbative origin and should decrease with rising Q^2 . The Cahn and Berger effects have opposite signs, but both increase in magnitude with z . The Berger effect should also increase in magnitude with x as the exclusive limit is approached, whereas the Cahn effect does not have any x dependence. To distinguish among these physical effects, one needs to perform a complete study of all kinematic dependencies in the data.

III. DATA ANALYSIS

The data were collected at Jefferson Lab in Hall B with CLAS [44] using a 0.354 g/cm² liquid-hydrogen target and a 5.75-GeV electron beam during the period October 2001 to January 2002. The average luminosity was 10³⁴ cm⁻² s⁻¹. CLAS is based on a six-sector torus magnet with its field pointing azimuthally around the beam direction. The torus polarity was set to bend negatively charged particles toward the beam line. The sectors delimited by the magnet coils are individually instrumented to form six independent magnetic spectrometers. The particle detection system includes drift chambers (DC) for track reconstruction [45], scintillation counters (SC) for time-of-flight measurements [46], Cherenkov counters (CC) for electron identification [47], and electromagnetic calorimeters (EC) for electron-pion separation [48]. The CLAS can detect and identify charged particles with momenta down to 0.2 GeV/ c for polar angles between 8° and 142°, while the electron-pion separation is limited up to about 50° by the CC acceptance. The total angular acceptance for electrons is about 1.5 sr. The CLAS superconducting coils limit the acceptance for charged hadrons to about 80% at $\theta = 90^\circ$ and about 50% at $\theta = 20^\circ$ (forward angles).

The electron momentum resolution is a function of the scattered electron angle and varies from 0.5% for $\theta \leq 30^\circ$ up to 1–2% for $\theta > 30^\circ$. The angular resolution is approximately constant, approaching 1 mrad for polar and 4 mrad for azimuthal angles. Therefore, the momentum transfer resolution ranges from 0.2 to 0.5%. For the present experiment the invariant mass of the struck proton ($W = \sqrt{(P+q)^2}$) has an estimated resolution of 2.5 MeV for beam energies less than 3 GeV and about 7 MeV for larger energies. In order to study all possible multiparticle states, we set the data acquisition trigger to require at least one electron candidate in any of the sectors, where an electron candidate was defined as the coincidence of a signal in the EC and Cherenkov modules for any one of the sectors.

A. Generic procedures

Both the e^- and π^+ were detected within the volume defined by fiducial cuts. These geometrical cuts selected regions of uniform high efficiency by removing areas near the detector boundaries and regions corresponding to problematic SC counters or DC readout. For electrons the fiducial volume limitations are mostly due to the Cherenkov counter, which is necessary for electron identification, and the electromagnetic calorimeter, which is used in the trigger. The CLAS Cherenkov counter's optics reduce significantly its azimuthal acceptance, in particular, in the region of small polar scattering angles, where the light collection mirrors are small. Moreover, the Cherenkov counter extends only up to $\sim 50^\circ$ in the polar scattering angle of an inbending charged particle. The trigger threshold for the electromagnetic calorimeter limits the lowest electron momentum, which in our case was about 0.64 GeV/c.

CLAS achieves its best charged-particle acceptance for π^+ , since complete identification requires only information from the drift chambers and the scintillation counters, which are limited in coverage only by the CLAS torus magnet's coils. For the standard torus configuration, π^+ particles bend outward toward larger angles, where the useful detector area between the coils is greater.

Small corrections to the momenta of the e^- and π^+ were necessary because of distortions in the drift chambers and magnetic fields not accounted for in the tracking routines. Correction parameters were determined by minimizing the difference in the missing mass for $ep \rightarrow ep$ and $ep \rightarrow e\pi^+n$ from known values (see Ref. [49]). The magnitude of these kinematic corrections was well below the CLAS resolution leading to subpercent changes in the measured cross section.

Events were selected by a coincidence of an electron and a π^+ whose identification criteria are described in the next section. The trigger gate time in CLAS was 150 ns, but, due to the limited range of particle momenta, the effective time window for a coincidence was much smaller. This, and the relatively low beam current in CLAS (about 7 nA), ensured that accidental coincidences were negligible.

B. Particle identification and backgrounds

The electron identification is based on combined information from the CC, EC, DC and SC. The fastest (as measured by the SC) negatively charged (as determined from DC tracking) particle having EC and CC hits is assumed to be an electron. However, the large rate of negatively charged pions contaminates the sample of reconstructed electrons, in particular, in the region of low momenta and large polar scattering angles. Moreover at lowest accessible polar scattering angles CC efficiency is reduced due to geometrical constraints. This contamination can be eliminated by using SC and DC information to better correlate the particle track and the time of the SC hit

with the CC signal [50]. We estimated the electron efficiency after this process to be greater than 97% and the corresponding inefficiency was propagated to e^- identification systematic uncertainty. The inefficiency is maximum at the lowest Q^2 .

The CC becomes less efficient at distinguishing electrons from pions for momenta above the Cherenkov light threshold for pions ($|\mathbf{p}| \approx 2.7$ GeV/c). However, in this kinematic region the EC signal can be used to remove the remaining pion contamination. The minimum-ionizing pion releases a nearly constant energy in the EC, independent of its momentum, whereas an electron releases an almost constant energy fraction of about 30% in the EC. Figure 4 shows a contour plot of events with momentum \mathbf{p} determined from the DC and total energy in the EC normalized by $|\mathbf{p}|$. Pion-electron separation, in this case, increases with particle momentum.

Pion identification is based on time of flight as measured with the SC and momentum as measured with the DC. Since the distance between the target and SC is independent of the scattering angle, the efficiency of pion identification depends only on the pion momentum and therefore on z . The time-of-flight resolution decreases with pion momentum leading to larger pion identification inefficiency. A contribution proportional to this inefficiency was added to π^+ identification systematic uncertainty. Furthermore, the time-of-flight interval between different hadron species decreases with hadron momentum resulting in larger contamination.

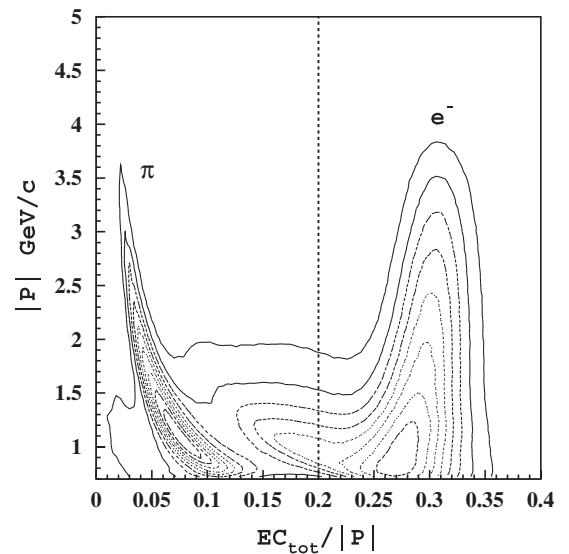


FIG. 4. Contour plot of particle momentum \mathbf{p} from tracking versus particle energy deposited in the calorimeter EC_{tot} normalized by $|\mathbf{p}|$. Events on the left correspond to pions and those on the right to electrons. Only fiducial cuts were applied. The Cherenkov detector, providing the basic electron identification, allows to identify clearly the electrons up to $|\mathbf{p}| \approx 2.7$ GeV/c. The dashed line shows the cut applied to the data to remove remaining pion contamination at $|\mathbf{p}| > 2.7$ GeV/c.

Figure 5 shows how effectively this procedure removes the background under the exclusive π^+n peak without a significant loss of good events. The example of the exclusive π^+n peak is important because these pions have large momenta, which makes their separation by time of flight more difficult than in the semi-inclusive case, where the pions have slightly lower momenta.

A positively charged particle identified as a pion may in some cases be a positron from e^+e^- pair production. This background becomes important at low momenta and at $\phi \approx 0$ or $\phi \approx 180^\circ$. To remove this contamination we applied the cut

$$M^2(e^-h^+) > 0.012 \exp[-M_{\text{TOF}}^4/(2\sigma_{\text{TOF}}^2)], \quad (14)$$

where M_{TOF} is the mass of the positive particle as measured by the TOF and $M(e^-h^+)$ is the invariant mass of the measured system of two particles in GeV/c^2 (assuming them to be e^+ and e^- and $\sigma_{\text{TOF}} = 0.01 (\text{GeV}/c^2)^2$). The remaining contribution from e^+e^- pairs is negligible over the entire kinematic range after the cut.

The electron, detected in coincidence with the pion, may be a secondary electron, whereas the scattered electron is not observed. To remove this background we measured lepton charge symmetric $e^+\pi^+$ coincidence cross section from the same data and removed its contribution from our data. This contamination is limited to a few lowest- x points where it achieves 5% at most.

Another source of contamination comes from K^+ production at high hadron momenta. At low hadron momenta the TOF system is able to distinguish pions from kaons, but above $|\mathbf{p}_h| \approx 1.2 \text{ GeV}/c$ the peaks of the two particles begin to mix. However, large hadron momenta make

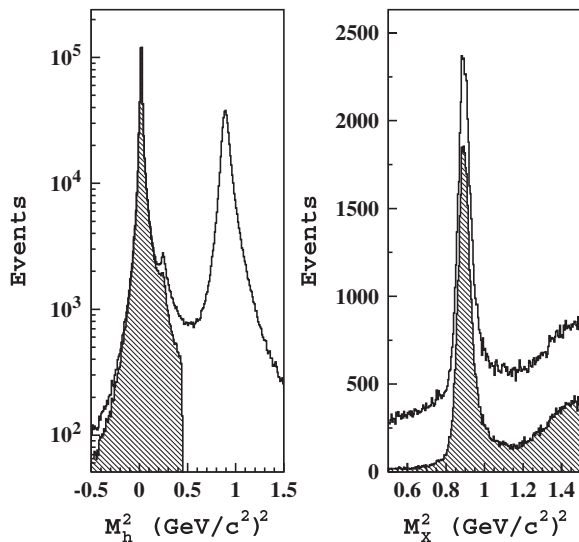


FIG. 5. Measured squared mass of positive hadrons (left) and squared missing mass for the e^-h^+ -system in the region of the π^+n exclusive peak (right). The shaded area indicates hadrons identified as pions. The exclusive π^+n was removed from the analysis by a cut $M_x^2 > 1.08 (\text{GeV}/c^2)^2$.

two-kaon production less likely due to the correspondingly high-energy threshold, and therefore most of the background comes from single kaons associated with Λ and Σ^0 production. In order to suppress the kaon contamination we applied two cuts: a kinematical cut that removes Λ , Σ^0 and $\Lambda^*(1520)$, and a TOF cut $M_h^2 < m_\pi^2 + 2\sigma_{M^2(\text{TOF})}$ that suppresses low-momentum kaons. The mass resolution of the TOF system was determined by fitting the width of the pion peak, which yielded $\sigma_{M^2(\text{TOF})} = 0.022|\mathbf{p}_h| \times \exp(0.6\sqrt{|\mathbf{p}_h|})$, where \mathbf{p}_h is given in GeV/c and $\sigma_{M^2(\text{TOF})}$ in $(\text{GeV}/c^2)^2$. Corrections for the remaining kaons from semi-inclusive production above the two-kaon threshold were made using the ratio of K^+ to π^+ semi-inclusive cross sections obtained from a pQCD-based Monte Carlo (MC) event generator (see the following section), weighted with the kaon/pion rejection factor obtained from the simulation itself. Kaons from the MC were propagated through the entire chain of the reconstruction procedure exactly in the same way as was done for pions, and the fraction $f(K^+)$ of kaons reconstructed as pions was obtained. This number was normalized to the fraction $f(\pi^+)$ of simulated pions reconstructed by the procedure. This kaon/pion rejection factor was parametrized as a function of the hadron momentum. The contribution from the K^+ background varied from 0 to 20% with an average of 1%, and our procedure reduced the kaons by a factor of 2 at 2.3 GeV/c with an increasing reduction factor at lower hadron momenta.

C. Empty target contribution

Empty target runs were analyzed in exactly in the same way as the full target runs and subtracted from the data to eliminate scattering from the target endcaps. The total charge collected on the empty target is an order of magnitude smaller than the one for the full target data. In order to increase the statistics of the empty target distributions, we made the assumption that the ratio of full to empty target event rates factorizes as a function of all variables. Thus one can obtain the ratio of empty to full target rates (ranging from 0 to 18% with an average value of 4.7%) for the five-fold differential cross section as a product of one-fold differential ratios. The contribution of empty target is typically smaller than the total systematic uncertainty, reaching its maximum at the two pion threshold.

D. Monte Carlo simulations

Detector efficiencies and acceptances were studied with a standard CLAS simulation package GSIM [51]. The simulated data obtained from GSIM can then be analyzed using the event reconstruction routine exactly in the same way as the measured data. This allows a complete determination of the detector efficiency plus acceptance.

The first step of the simulation is to generate $e^-\pi^+$ coincidence events based on a pQCDlike SIDIS param-

trization [52] at leading order for the semi-inclusive contribution and on the MAID2003 model [53] extrapolated to the $W > 2 \text{ GeV}/c^2$ region with the parametrization from Ref. [54] for the exclusive $\pi^+ n$ reaction. Distributions of counts from the experimental data and GSIM simulations are shown in Fig. 6. The same cuts are applied to both data and MC as described in the previous section.

The MC yield reproduces the shape of the experimental data fairly well. In order to keep systematic uncertainties on the acceptance plus efficiency small (we estimated them to be 10%) we had to extract fully differential cross sections in narrow kinematic bins. Bins with combined acceptance and efficiency $< 0.1\%$, corresponding to 25% filling per each dimension, were discarded. The average value of combined acceptance and efficiency was about 25%.

To test Monte Carlo simulations of electrons we extracted the inclusive structure function F_2 and compared it to the world data in our kinematic range. An example of this comparison at $Q^2 = 2 \text{ (GeV}/c^2)^2$ is shown in Fig. 7.

For positively charged hadrons we tested Monte Carlo simulations by extracting the elastic scattering cross sec-

tion measured in electron-proton coincidences. The normalized event yield was compared to normalized GSIM simulation yield, based on form-factors from Ref. [55]. The obtained ratio, shown in Fig. 8, is in good agreement with unity in the central region of Q^2 , but rises at large Q^2 due to unresolved inelastic contamination.

Furthermore, the efficiency of π^+ production reconstruction in the present data set was tested in the measurement of the exclusive pion production published in Ref. [49].

E. Binning

The data were divided into kinematic bins as follows:

- (i) Q^2 – 10 logarithmic bins (with centers at) 1.31–1.56 (1.49), 1.56–1.87 (1.74), 1.87–2.23 (2.02), 2.23–2.66 (2.37), 2.66–3.17 (2.93), 3.17–3.79 (3.42), 3.79–4.52 (4.1), 4.52–5.4 (4.85), 5.4–6.45 (5.72), 6.45–7.7(6.61) $(\text{GeV}/c)^2$;
- (ii) x – 25 logarithmic bins in the interval from 0.01 to 1;
- (iii) z – 25 logarithmic bins in the interval from 0.01 to 1;

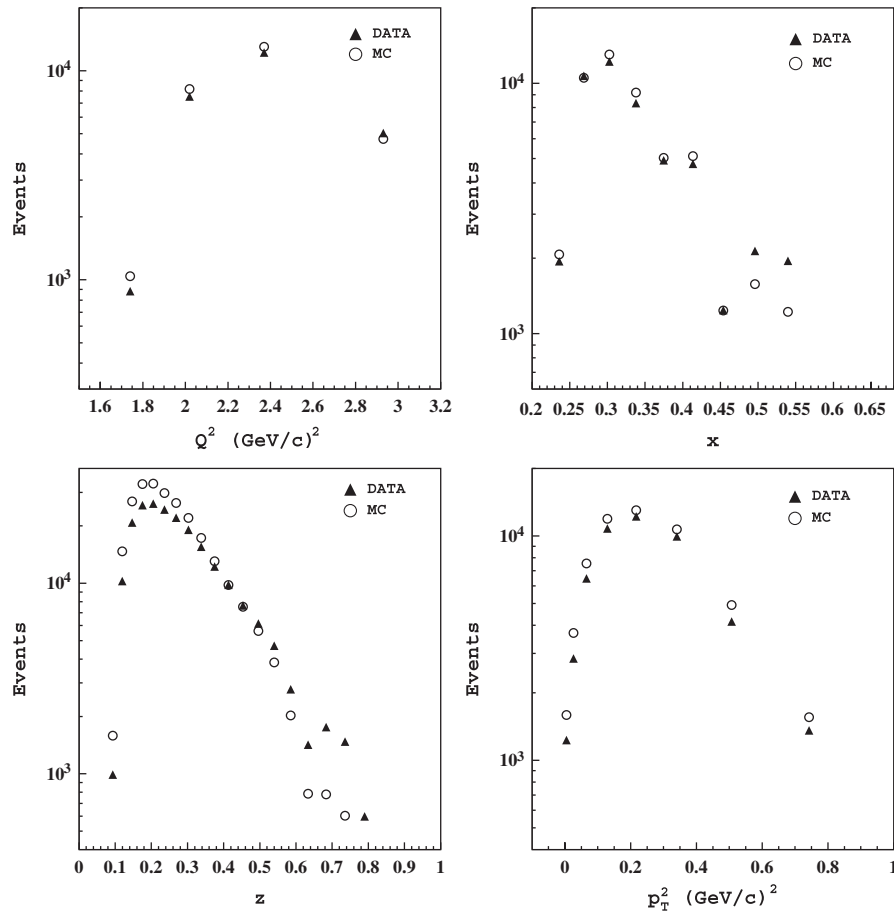


FIG. 6. Comparison of $e^- \pi^+$ coincidence data (full triangles) and MC raw yields (open circles) as a function of one of the kinematic variables. The other variables were kept fixed at $Q^2 = 2.4 \text{ (GeV}/c^2)^2$, $x = 0.30$, $z = 0.37$, $p_T^2 = 0.22 \text{ (GeV}/c^2)^2$. The MC simulation yield was normalized to the integrated luminosity of the experiment. Error bars are statistical only and they are smaller than the symbol size.

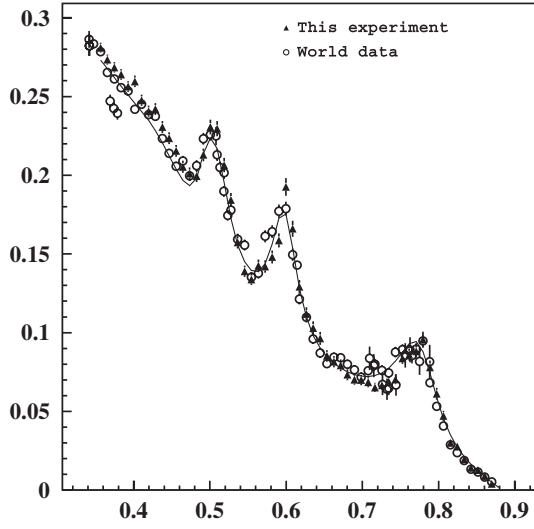


FIG. 7. Inclusive structure function F_2 at $Q^2 = 2$ (GeV/c) 2 extracted from the present experiment (full triangles) in comparison with previous world data (open circles) from Ref. [77] and references therein. The curve is a parametrization from Ref. [77]. The error bars are statistical only and an overall systematic uncertainty for the present experiment of the order or 5% is estimated.

- (iv) p_T – 10 logarithmic bins (with centers at): 0–0.1 (0.07), 0.1–0.2 (0.16), 0.2–0.3 (0.26), 0.3–0.41 (0.36), 0.41–0.53 (0.47), 0.53–0.65 (0.58), 0.65–0.8

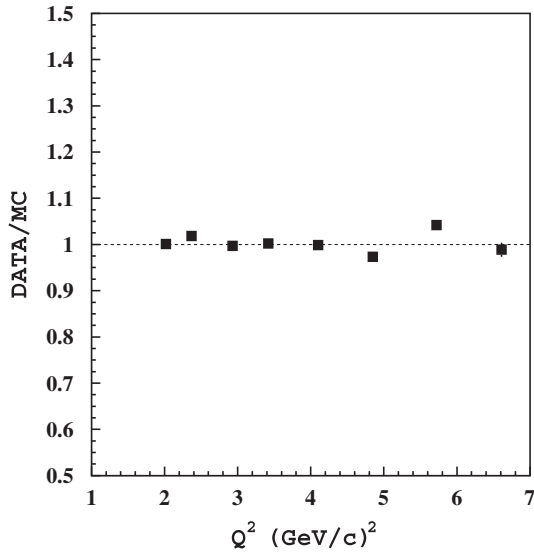


FIG. 8. Ratio of e^-p coincidence events from the data and GSIM Monte Carlo simulations. The simulation event generator was based on proton form-factors from Ref. [55]. The coincidences were selected by the following set of cuts: $|W^2 - M^2| < 0.2$ (GeV/c) 2 , $|M_x^2| < 0.01$ (GeV/c) 2 and $|\phi_h - \phi_e - \pi| < 4$ degrees. The error bars are statistical only and an overall systematic uncertainty of the order or 10% is estimated. Error bars are smaller than the symbol size.

$$(0.71), \quad 0.8-0.97 \quad (0.86), \quad 0.97-1.22 \quad (1.04), \\ 1.22-1.64(1.25) \text{ GeV}/c;$$

(v) ϕ – 18 linear bins in the interval from 0 to 360°. The bin sizes were chosen large enough to accommodate CLAS angular and momentum resolutions reducing bin migrations, but they were small enough to avoid reconstruction efficiency model dependence. Indeed the average bin migration is about 30%, consistent with expectation for bin size close to 1σ of detector resolution. The centers of the Q^2 and p_T bins coincide with the mean values of these variables in the raw data after all cuts but before acceptance corrections.

The general rectangular grid described above was used to sort the data. But the measured kinematic volume is not rectangular. Hence a fraction of bins in one dimension can be out of the accessible range depending on the values of the other four variables. This is, in particular, the case when one of variables is close to the kinematic limits of the accessible region.

F. Five-fold differential cross section

The five-fold differential semi-inclusive cross section was extracted for each kinematic bin from the number of measured events N_{dat} according to the relation:

$$\frac{d^5\sigma}{dx dQ^2 dz dp_T^2 d\phi} = \frac{G_{\text{dat}}}{\Delta x \Delta Q^2 \Delta z \Delta p_T^2 \Delta \phi} \\ \times \frac{N_{\text{dat}}(x, Q^2, z, p_T^2, \phi)}{F_{\text{eff/acc}}(x, Q^2, z, p_T^2, \phi)}, \quad (15)$$

with data inverse luminosity given by

$$G_{\text{dat}} = \frac{1}{\mathcal{L}} = \frac{1}{\rho \frac{N_A}{M_A} L Q_{\text{FC}}}, \quad (16)$$

$\rho = 0.0708$ g/cm 3 is the liquid-hydrogen target density, $L = 5$ cm is the target length and Q_{FC} is the total charge collected in the Faraday Cup (FC), corrected for dead time. $F_{\text{eff/acc}}(x, Q^2, z, p_T^2, \phi)$ is the acceptance/efficiency correction obtained with Monte Carlo simulations:

$$F_{\text{eff/acc}}(x, Q^2, z, p_T^2, \phi) = \frac{G_{\text{sim}}}{\Delta x \Delta Q^2 \Delta z \Delta p_T^2 \Delta \phi} \\ \times \frac{N_{\text{rec}}(x, Q^2, z, p_T^2, \phi)}{\sigma_M(x, Q^2, z, p_T^2, \phi)}, \quad (17)$$

with its normalization factor given by

$$G_{\text{sim}} = \frac{\int_{\tau} d\sigma_M}{N_{\text{tot}}}. \quad (18)$$

Here $N_{\text{rec}}(x, Q^2, z, p_T^2, \phi)$ is the number of Monte Carlo events reconstructed in the current bin, $\sigma_M(x, Q^2, z, p_T^2, \phi)$ is the cross section model used in the event generator, τ is the complete phase space volume of event generation and N_{tot} is the total number of generated events.

The final cross sections were corrected for radiative effects using the analytic calculations described in Refs. [52,56] implemented in the Monte Carlo generator. It includes both radiative corrections to the SIDIS spectrum and the radiative tail from exclusive π^+n production. The average contribution of radiative corrections is about 6% with largest contribution close to the two-pion threshold. The magnitude of radiative corrections increases with z and p_T^2 .

G. Azimuthal dependence

A separation of the constant, $\cos\phi$ and $\cos 2\phi$ terms in Eq. (1) has been performed using two methods, either a fit to the ϕ -distributions or an event-by-event determination of azimuthal moments. Both methods should give compatible results. By studying the two methods in detail we concluded that both give unreliable results if the ϕ -distribution contains regions of poor detector acceptance. Therefore we excluded kinematic points where the ϕ -acceptance was inadequate. This reduced significantly the kinematic range of the extracted moments. Nevertheless, the kinematic bins with incomplete ϕ -coverage can still be used in a multidimensional fit exploiting continuity in the other variables.

In the first method we fit the ϕ -distribution to the function $\sigma_0(1 + 2B \cos\phi + 2C \cos 2\phi)$ using MINUIT [57] and extracted the coefficients σ_0 , B and C and their statistical uncertainties. These coefficients give the ϕ -integrated cross section, $\langle \cos\phi \rangle$ and $\langle \cos 2\phi \rangle$, respectively.

The second method of moments was used in a previous CLAS paper [58], but due to the strong effect of acceptance on even moments, we developed the necessary corrections described below. The fully differential cross section can be written as

$$\sigma = V_0 + V_1 \cos\phi + V_2 \cos 2\phi. \quad (19)$$

The acceptance/efficiency correction can be expanded in a Fourier series in ϕ as

$$F_{\text{eff/acc}} = \frac{A_0}{2} + \sum_{n=1}^{\infty} A_n \cos n\phi + \sum_{n=1}^{\infty} B_n \sin n\phi. \quad (20)$$

The coefficients B_n are fairly small in CLAS. Fourier spectrum of the raw data and MC yields is shown in Fig. 9.

Let us define the Fourier coefficients of raw yield (before acceptance/efficiency correction)

$$Y_n = \frac{1}{\pi} \int_0^{2\pi} \tilde{\sigma}(\phi) \cos n\phi d\phi, \quad (21)$$

where $\tilde{\sigma} = F_{\text{eff/acc}}\sigma$ is the cross section distorted by the acceptance/efficiency correction $F_{\text{eff/acc}}$. Then combining Eqs. (19)–(21) we obtain an infinite series of linear equations relating Fourier coefficients of the raw yield and the physical cross section:

$$Y_n = A_n V_0 + \frac{A_{n-1} + A_{n+1}}{2} V_1 + \frac{A_{n-2} + A_{n+2}}{2} V_2, \quad (22)$$

where $A_n = A_{-n}$ and $n = 0, 1, 2, \dots$. The magnitudes of A_n and Y_n decrease rapidly with n and are consistent with zero for $n > 10$ (see Fig. 9). As one can see in the figure the Monte Carlo simulations describe fairly well Fourier spectrum of the data, in particular, for large n . Therefore, we can cut the infinite set of equations for MC Y_n at some arbitrary $n = N$ and solve the resulting system of N linear equations to obtain A_n coefficients for $n = 0, 1, 2, \dots, N$. Assuming that GSIM reproduces the CLAS acceptance and efficiency (within systematic uncertainties treated later), coefficients A_n should be the same as in the data. We used these efficiency/acceptance Fourier coefficients A_n in the expression for data Y_n to extract the measured cross section ϕ -terms: V_0 , V_1 and V_2 . We fit the over-determined system of N linear equations with these 3 unknowns using the weighted linear least squares fitting routine TLS in the CERNLIB library [57].

The stability of the solution as a function of N is shown in Fig. 10. From this plot we concluded that $N = 7$ is the minimum number of moments necessary to extract sensible $\langle \cos\phi \rangle$ and $\langle \cos 2\phi \rangle$ for the present kinematics. In the following we made the more conservative choice of $N = 20$.

A typical acceptance-corrected ϕ -distribution is shown in Fig. 11 together with the two methods of extracting moments, which are in good agreement. The systematic uncertainties on the ϕ -dependent terms are larger than the difference between the two methods (see the following section).

The acceptance correction was also tested by dividing each bin in two parts by cutting the corresponding scattered

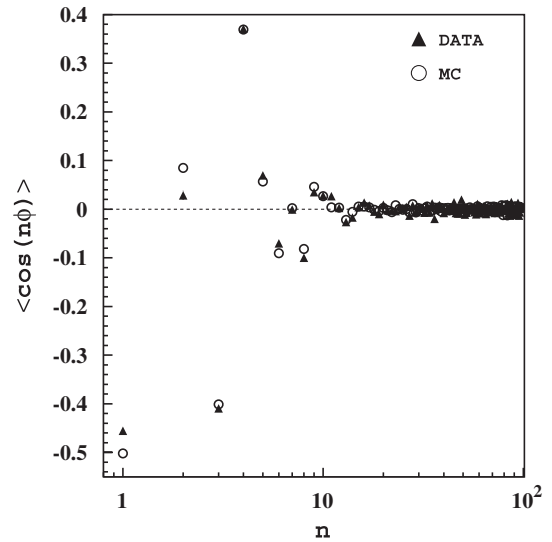


FIG. 9. Extracted Fourier components of the raw data (full triangles) and the Monte Carlo (open circles) yields. Error bars are statistical only and they are smaller than the symbol size.

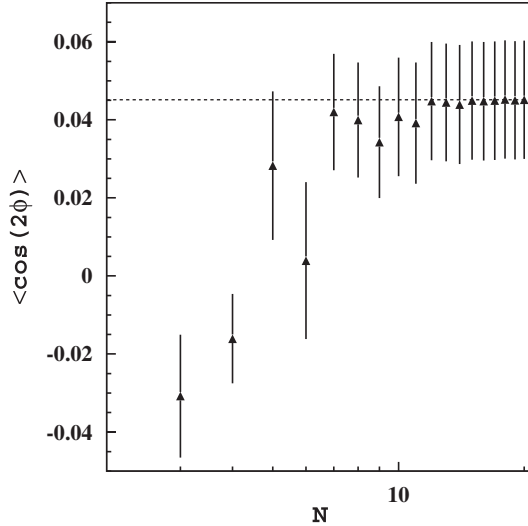


FIG. 10. Stability of the V_2 cross section term as a function of the number of moments N taken into account in the extraction procedure. Error bars are statistical only.

electron energy range in two equal intervals and comparing the extracted $\langle \cos\phi \rangle$ and $\langle \cos 2\phi \rangle$ terms in these two acceptance regions. An example of this test is shown in Figs. 12 and 13. It can be seen that the acceptance corrections are significant and sometimes differ for the two separated regions, however the final reconstructed $\langle \cos\phi \rangle$ and $\langle \cos 2\phi \rangle$ comes out to be consistent within statistical and systematic uncertainties.

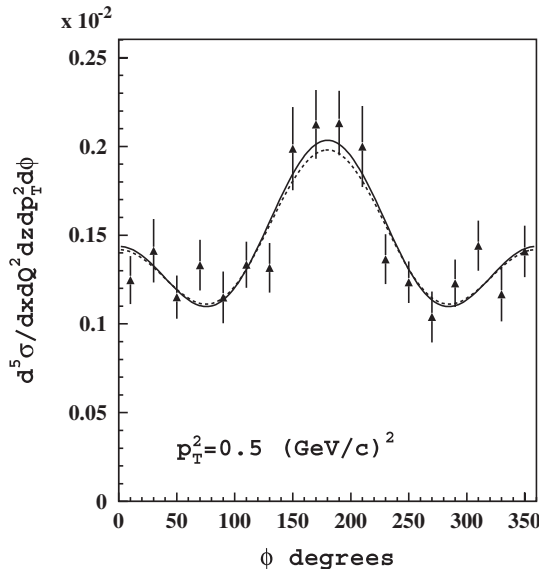


FIG. 11. The ϕ -dependence of the data taken at $Q^2 = 2 \text{ (GeV/c)}^2$, $x = 0.24$, $z = 0.18$ and $p_T^2 = 0.5 \text{ (GeV/c)}^2$ (full triangles) together with the results of the azimuthal moment (solid lines) and fitting (dashed line) methods. Error bars are statistical only.

H. Systematic uncertainties

The systematic uncertainties for the measured absolute cross sections are considerably different from those for the azimuthal moments, because many quantities drop out in the ratios measured by moments. Most of systematic uncertainties are point-to-point correlated and evaluated on a bin-by-bin basis with the exception of the overall normalization, efficiency, and radiative and bin-centering corrections, for which a uniform relative uncertainty was assumed. The following sections discuss these uncertainties.

1. Cross section

The total systematic uncertainties on the five-fold differential cross section vary from 11 to 44% with a mean value of 16%. Apart from systematics due to the efficiency corrections discussed in Sec. III D, the major contributions come from detector acceptance and electron identification. The relative value of most uncertainties is amplified at the two-pion threshold, where the cross section vanishes.

The estimate of the systematic uncertainty from efficiency modeling comes from a comparison of cross section extractions using two different event generators: one uses a LO pQCD model, while the other is based on the sum over several exclusive channels.

The systematic uncertainties on the acceptance were estimated from the variation in the absolute cross sections obtained using each of six CLAS sectors separately to

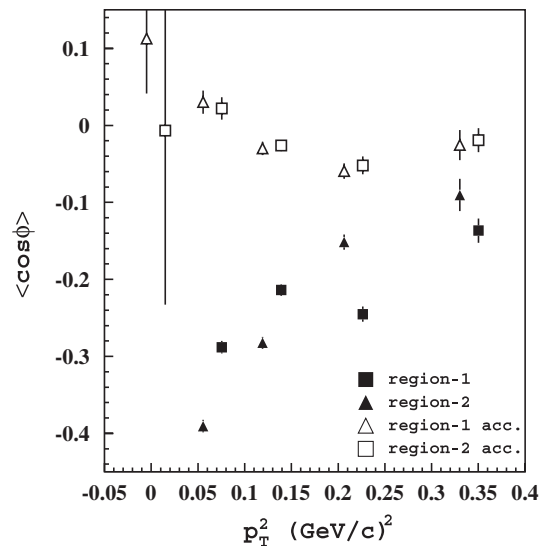
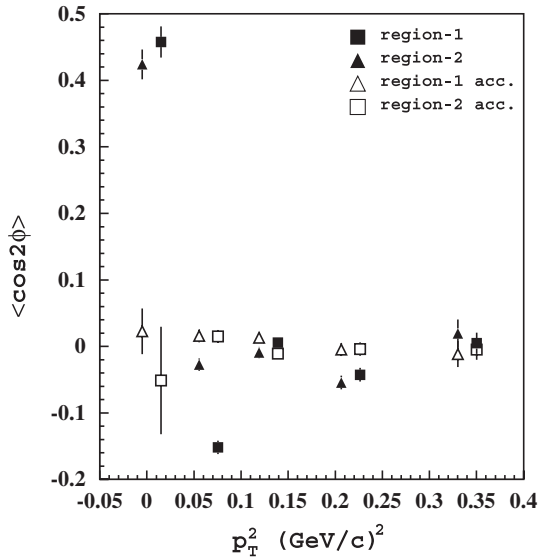


FIG. 12. The p_T^2 -dependence of the $\langle \cos\phi \rangle$ taken at $Q^2 = 2 \text{ (GeV/c)}^2$, $x = 0.30$ and $z = 0.21$ obtained from two different detector acceptance regions (triangles and squares). Full markers correspond to the data before the acceptance correction and the empty markers show acceptance-corrected $\langle \cos\phi \rangle$. The two data sets are shifted equally along the x -axis in opposite directions from their central values for visibility. Error bars are statistical only.

FIG. 13. Same as Fig. 12 except for $\langle \cos 2\phi \rangle$.

detect the electron (pion) and then integrating over the pion (electron) wherever else it appeared. This uncertainty was estimated bin-by-bin and reflects the ability of Monte Carlo to describe the detector nonuniformities. The uncertainty increases at a low polar scattering angle, and therefore low- Q^2 for electrons and low- p_T^2 for pions, where the azimuthal acceptance of CLAS is reduced.

Systematic uncertainties arising from electron identification were estimated by comparing two different methods (as in Ref. [50]) of pion rejection, one based on Poisson shapes of Cherenkov counter spectra and another on the geometrical and temporal matching between the measured track and Cherenkov signal. This uncertainty appears mostly at low- Q^2 , where CC is less efficient.

The systematic uncertainty arising from π^+ identification has two contributions. One was estimated from the difference between the ratios of events in the missing neutron peak before and after pion identification as calculated for data and GSIM simulations. The second part comes from our treatment of kaon contamination which was assumed to be 20%. The two errors were added in quadrature.

Radiative corrections are model-dependent. To estimate this systematic uncertainty we changed the model used in the radiative correction code by 15% and took the resulting difference as an estimate of the uncertainty.

There is an additional overall systematic uncertainty of 1% due to uncertainties in the target length and density. The target length was 5 ± 0.05 cm and the liquid-hydrogen density was $\rho = 0.0708 \pm 0.0003$ g/cm³ giving approximately a 1% uncertainty.

The systematic uncertainty on the bin-centering correction was estimated in the same way as for the radiative corrections. The model was changed as described above and the difference between the two centering corrections was taken as the uncertainty.

The empty target subtraction introduces a small systematic uncertainty due to the assumption of cross-section-ratio (empty to full target) factorization in the individual kinematic variables. This uncertainty was estimated by comparing the factorized and direct bin-by-bin subtraction methods.

These main contributions are listed in Table I. All systematic uncertainties shown in the table were combined in quadrature.

2. Azimuthal moments

Azimuthal moments (see Eq. (3)) have the advantage of smaller systematic uncertainties since many of them cancel in the ratio. In particular, systematic uncertainties of overall normalization, kinematic corrections, particle identification, efficiency, empty target subtraction and bin centering cancel. The remaining systematic uncertainties are due to nonuniformities in the CLAS acceptance and radiative corrections. The uncertainties due to CLAS acceptance were estimated as the spread between the central values of the azimuthal moments obtained using each single CLAS sector to detect the electron or pion and then integrating over the second particle (pion and electron, respectively). This way we obtained the influence of the electron and pion acceptances separately. Similar conclusions about the acceptance influence on the azimuthal moment extraction were made in Ref. [59].

To estimate the systematic uncertainties of the radiative corrections, we made a few calculations in randomly chosen kinematic points comparing correction factors obtained with our model, changing by 15% the exclusive π^+n contribution or modifying by 30% the \mathcal{H}_3 and \mathcal{H}_4 structure functions. The difference in the correction factor was taken as the estimate of this systematic uncertainty. The variation range and averaged value of these systematic uncertainties are given in Tables II and III for the $\langle \cos\phi \rangle$ and $\langle \cos 2\phi \rangle$ moments, respectively.

TABLE I. Systematic uncertainties of the semi-inclusive cross section.

Source	Variation range %	Mean value %
Overall normalization	1	1
e^- identification	1.8–13	3.5
π^+ identification	0.9–6.7	2.1
e^- acceptance	0–19	5.3
π^+ acceptance	0–52	4
Efficiency	10	10
Radiative corrections	2	2
Empty target subtraction	0–0.7	0.2
Bin-centering correction	0.7	0.7
Total	11–54	14

TABLE II. Systematic uncertainties of $\langle \cos\phi \rangle$.

Source	Variation range	Mean value
e^- acceptance	0–0.06	0.016
π^+ acceptance	0–0.13	0.016
Radiative corrections	0.005	0.005
Total	0.005–0.13	0.026

TABLE III. Systematic uncertainties of $\langle \cos 2\phi \rangle$.

Source	Variation range	Mean value
e^- acceptance	0–0.08	0.015
π^+ acceptance	0–0.12	0.011
Radiative corrections	0.003	0.003
Total	0.003–0.12	0.021

TABLE IV. Additional systematic uncertainty on \mathcal{H}_2 .

Source	Variation range %	Mean value %
R ratio	0.6–1.9	1.5

3. Structure functions

One additional systematic uncertainty appears in the extraction of the structure function \mathcal{H}_2 from the measured combination $\mathcal{H}_2 + \epsilon\mathcal{H}_1$. In this case some transverse to longitudinal cross section ratio R should be assumed. In our results on the structure function \mathcal{H}_2 we included a 50% systematic uncertainty on R . This does not affect strongly the extracted structure function \mathcal{H}_2 (see Eq. (2)), in the same way as the inclusive structure function F_2 is weakly sensitive to the ratio R for forward-angle scattering. The assumed 50% precision leads to the systematic uncertainty shown in the Table IV.

IV. RESULTS

The obtained data allow us to perform studies in four different areas: hadron transverse momentum distributions, comparison of the ϕ -independent term with pQCD calculations, search for the target fragmentation contribution and study of azimuthal moments. We present these analyses in the following sections.

A. Transverse momentum distributions

The ϕ -independent part of the cross section falls off exponentially in p_T^2 , as shown in Fig. 14. This has been predicted in Ref. [31] to arise from the intrinsic transverse momentum of partons. We observe no deviation from this exponential behavior over the entire kinematic domain of our data.

By studying the p_T^2 -dependence in our data at various values of z , we have extracted the z -dependence of the mean transverse momentum $\langle p_T^2 \rangle$, defined within the

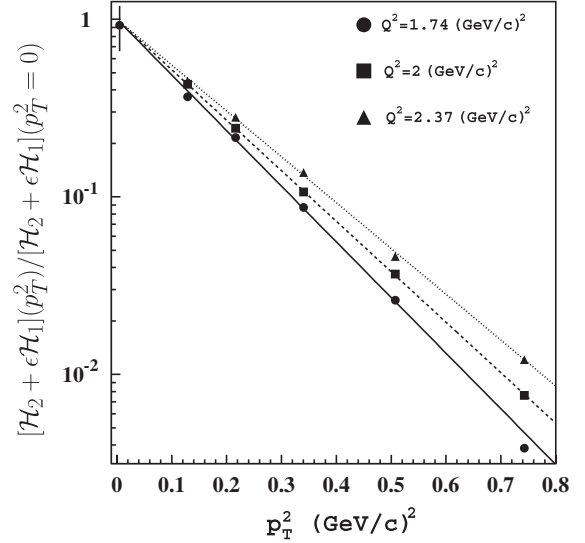


FIG. 14. The p_T^2 -dependence of the ϕ -independent term $\mathcal{H}_2 + \epsilon\mathcal{H}_1$ at $x = 0.24$ and $z = 0.30$. The lines represent exponential fits to the data for $Q^2 = 1.74$ (GeV/c) 2 (full circles and solid line), $Q^2 = 2$ (GeV/c) 2 (full squares and dashed line), and $Q^2 = 2.37$ (GeV/c) 2 (triangles and dotted line). The errors bars are statistical only.

Gaussian model, in Eq. (7), and obtained by fitting p_T^2 -distributions in each (x, Q^2, z) bin. Figure 15 shows a clear rise of $\langle p_T^2 \rangle$ with z . We compared this with the distribution given in Eq. (8) with $a^2 = 0.25$ and $b^2 = 0.20$ (GeV/c) 2 based on previous data [32–34]. Significant deviations from this behavior were found at low- z , which can be explained as a threshold kinematic effect. The maximum achievable transverse momentum $p_T^{\max} \simeq z\nu$ becomes smaller at low z , because ν is limited by the 5.75-GeV beam energy, and p_T^{\max} is smaller than the intrinsic transverse momentum of partons which is at first order independent of beam energy. This leads to a cut on the p_T^2 -distribution, which is not present in high-energy experiments. To account for this low-energy effect we modified the parametrization as

$$\langle \tilde{p}_T^2 \rangle = \frac{\langle p_T^2 \rangle}{1 + \langle p_T^2 \rangle / (p_T^2)^{\max}}. \quad (23)$$

The dotted curve in Fig. 15 shows that this new parametrization follows the data points, but the absolute normalization given by the parameters a and b is still too high. This modification breaks the factorization between x , Q^2 and p_T in the low- z region because the p_T^2 -distribution now depends also on x and Q^2 .

At large z , p_T^{\max} is also large. Therefore, we can check the factorization of p_T^2 from x and Q^2 . Figure 16 shows no appreciable dependence of the mean transverse momentum $\langle p_T^2 \rangle$ for $x < 0.5$ corresponding to the missing mass $M_X^2 < 1.6$ (GeV/c) 2 , i.e. the Δ resonance region.

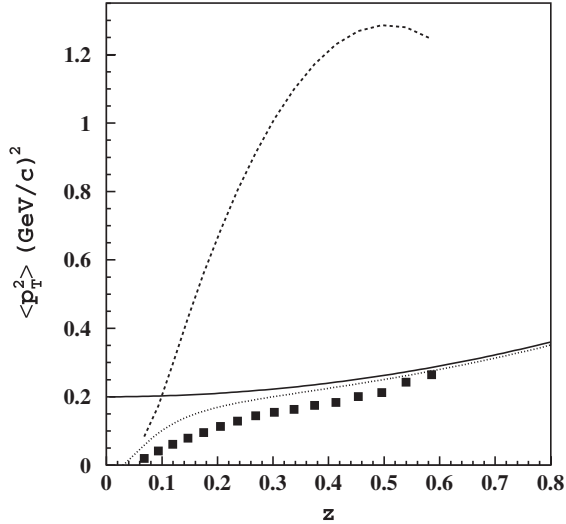


FIG. 15. The z -dependence of $\langle p_T^2 \rangle$ at $Q^2 = 2.37$ (GeV/c) 2 and $x = 0.27$. The points are the data from the present analysis. The curves show the maximum allowed $p_T^2 = (p_T^2)^{\max}$ (dashed), the parametrization of high-energy data from Eq. (8) (solid), and the low- z modification from Eq. (23). The error bars are statistical only and they are smaller than the symbol size.

The transverse momentum distribution exhibits a small variation with Q^2 over the covered kinematic interval as seen in the different slopes in Fig. 14. However, the Q^2 coverage is insufficient to observe the logarithmic pQCD evolution of $\langle p_T^2 \rangle$ with Q^2 discussed in Ref. [60].

B. Comparison with pQCD

In order to compare the ϕ -independent term with pQCD predictions, we assumed a constant longitudinal to transverse cross section ratio $R = 0.12$ [21].

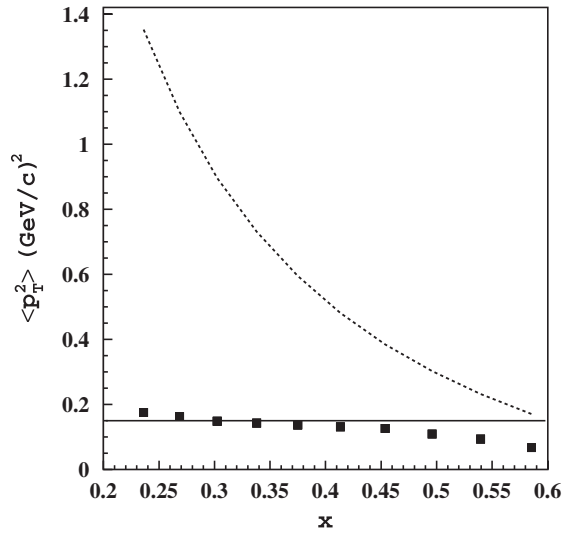


FIG. 16. The x -dependence of $\langle p_T^2 \rangle$ at $Q^2 = 2.37$ (GeV/c) 2 and $z = 0.34$. The points are from the present analysis. The curves show $p_T^2 = (p_T^2)^{\max}$ (dashed) and a constant fit to the data (solid). The error bars are statistical only.

Since there is no TMD-based approach to which we could directly compare our data, we integrated the measured structure functions \mathcal{H}_2 in p_T^2 in order to compare \mathcal{H}_2 measured in this experiment with H_2 from pQCD calculations. We integrated Eq. (1) in ϕ and p_T^2 and compared with Eq. (4) obtaining

$$H_2(x, Q^2, z) = \pi E_h \int_0^{(p_T^2)^{\max}} dp_T^2 \frac{\mathcal{H}_2(x, z, Q^2, p_T)}{\sqrt{E_h^2 - m_h^2 - p_T^2}}, \quad (24)$$

where the upper limit of integration is given by the smaller of the quantities $(p_T^2)^{\max} = (z\nu)^2 - m_h^2$ and the value defined by the pion threshold, which limits the longitudinal hadron momentum in the lab frame to

$$p_{\parallel} > p_{\parallel}^{\min} = \frac{1}{2|\mathbf{q}|} \{ (M_n^2 - M^2) + Q^2 - 2M\nu(1-z) - m_{\pi}^2 + 2zv^2 - 2M_n m_{\pi} \}. \quad (25)$$

This limits $p_T^2 < |\mathbf{p}_h|^2 - (p_{\parallel}^{\min})^2$. If we exploit the exponential behavior of the measured structure function \mathcal{H}_2 in p_T^2 (see Eq. (7)), the integration can be performed analytically leading to

$$H_2(x, Q^2, z) = V(x, Q^2, z) E_h e^{-\langle |\mathbf{p}_h|^2 / \langle p_T^2 \rangle \rangle} \sqrt{\frac{\pi}{\langle p_T^2 \rangle}} \left[\text{Erfi} \left(\sqrt{\frac{|\mathbf{p}_h|^2}{\langle p_T^2 \rangle}} \right) - \text{Erfi} \left(\sqrt{\frac{|\mathbf{p}_h|^2 - (p_T^2)^{\max}}{\langle p_T^2 \rangle}} \right) \right], \quad (26)$$

where $V(x, Q^2, z)$ is the p_T -independent part of the structure function and Erfi is the imaginary error function. By neglecting the factor $E_h/|\mathbf{p}_{\parallel}|$ in Eq. (1) and by extending the integral to infinity (as typically done in SIDIS analyses, see Eq. (7)), we find

$$H_2(x, Q^2, z) = V(x, Q^2, z). \quad (27)$$

In Figs. 17–20 our integrated structure function H_2 is compared to pQCD calculations given by

$$H_2(x, Q^2, z) = \int_x^1 \frac{d\xi}{\xi} \int_z^1 \frac{d\zeta}{\zeta} \sum_{ij} \sigma_{\text{hard}}^{ij} \left(\xi, \zeta, \frac{Q^2}{\mu^2}, \alpha_s(\mu^2) \right) \times \frac{x}{\xi} f_i \left(\frac{x}{\xi}, \mu^2 \right) \frac{z}{\zeta} D_j^{\pi^+} \left(\frac{z}{\zeta}, \mu^2 \right), \quad (28)$$

where $\sigma_{\text{hard}}^{ij}$ is the hard scattering cross section for incoming parton i and outgoing parton j given in Ref. [61], f_i is the parton distribution function for parton i taken from Ref. [23], $D_j^{\pi^+}$ is the fragmentation function for parton j and hadron π^+ taken from Ref. [26], and μ is the factorization/renormalization scale. These next-to-leading order (NLO) calculations include a systematic uncertainty due to arbitrary factorization/renormalization scale variations [62], indicating the size of possible higher-order effects. This was evaluated by variation of each scale by a factor of 2 in both directions and the obtained differences for all

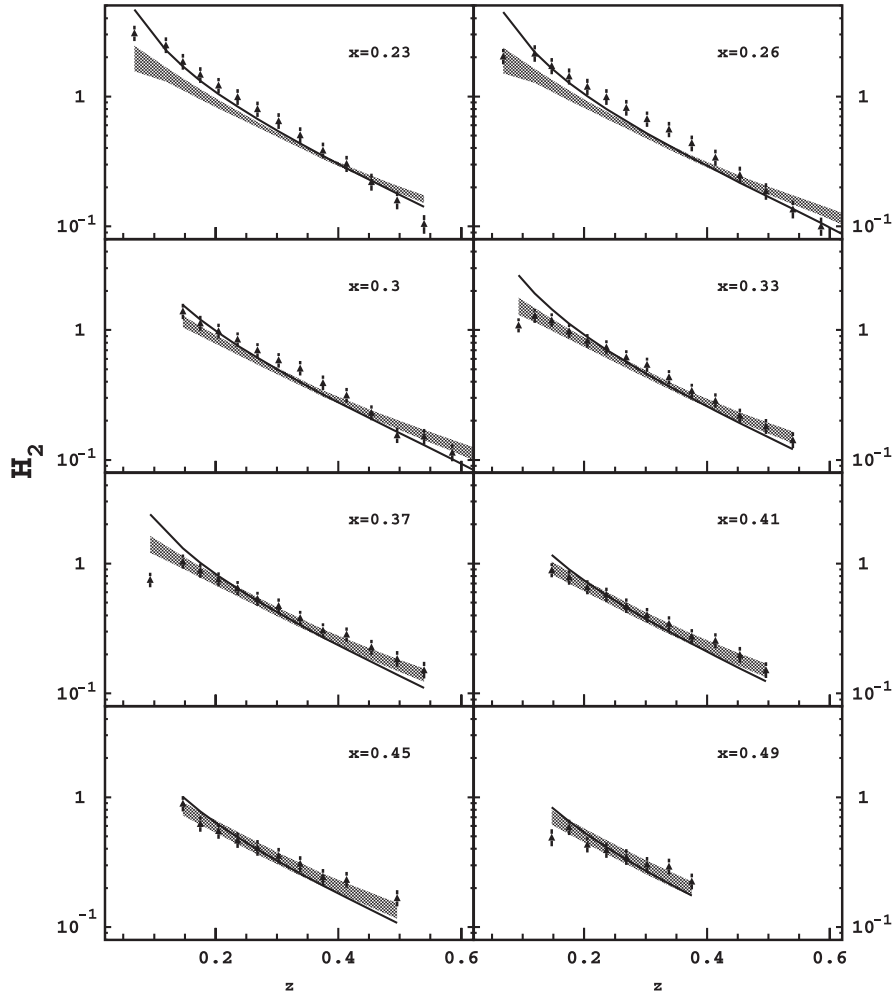


FIG. 17. The z -dependence of H_2 at $Q^2 = 2.37$ (GeV/c) 2 . The data are shown by full triangles. The error bars give statistical and systematic uncertainties combined in quadrature. The solid line shows LO pQCD calculations using the prescription from Ref. [61], CTEQ 5 parton distribution functions [23], and the Kretzer fragmentation functions [26]. NLO calculations performed within the same framework (using CTEQ 5M PDFs) are shown by the shaded area, for which the width indicates systematic uncertainties due to factorization and renormalization scale variations [62].

scales were summed in quadrature. NLO calculations within their uncertainty lie closer to the data in the low- z region than leading-order ones. The difference between the data and NLO pQCD is at most about 20%. At low x and $z < 0.4$ the data are higher than NLO calculations, while at largest x both the LO and NLO calculations lie above the data. The multiplicity ratio H_2/F_2 shown in Fig. 21 demonstrates the same level of agreement between data and pQCD calculations as H_2 alone. This suggests that the differences between the data and theory do not cancel in the ratio.

The widening systematic uncertainty band in the NLO calculations at high x suggests that the discrepancy with the data here might be due to a significant contribution from multiple soft gluon emission, which can be resummed to all orders in α_s as in Refs. [63,64]. Similar results were obtained in Ref. [65] from the comparison between HERMES π^+ SIDIS data and NLO calculations.

The difference between the data and calculations in some kinematic regions leaves room for an additional contribution from target fragmentation of $<20\%$. However, the possible presence of higher twists at our relatively small Q^2 values casts doubt on the attribution of data/pQCD differences to target fragmentation. In order to better explore target fragmentation, we studied the t and x_F -dependencies of \mathcal{H}_2 as described in the following section.

The pQCD calculations are significantly biased by the assumption of favored fragmentation [26]. In fact, using unseparated $h^+ + h^-$ fragmentation functions as directly measured in e^+e^- collisions, one obtains curves that are systematically higher by about 20%.

C. Target fragmentation

In leading-order pQCD, the structure function H_2 is given by

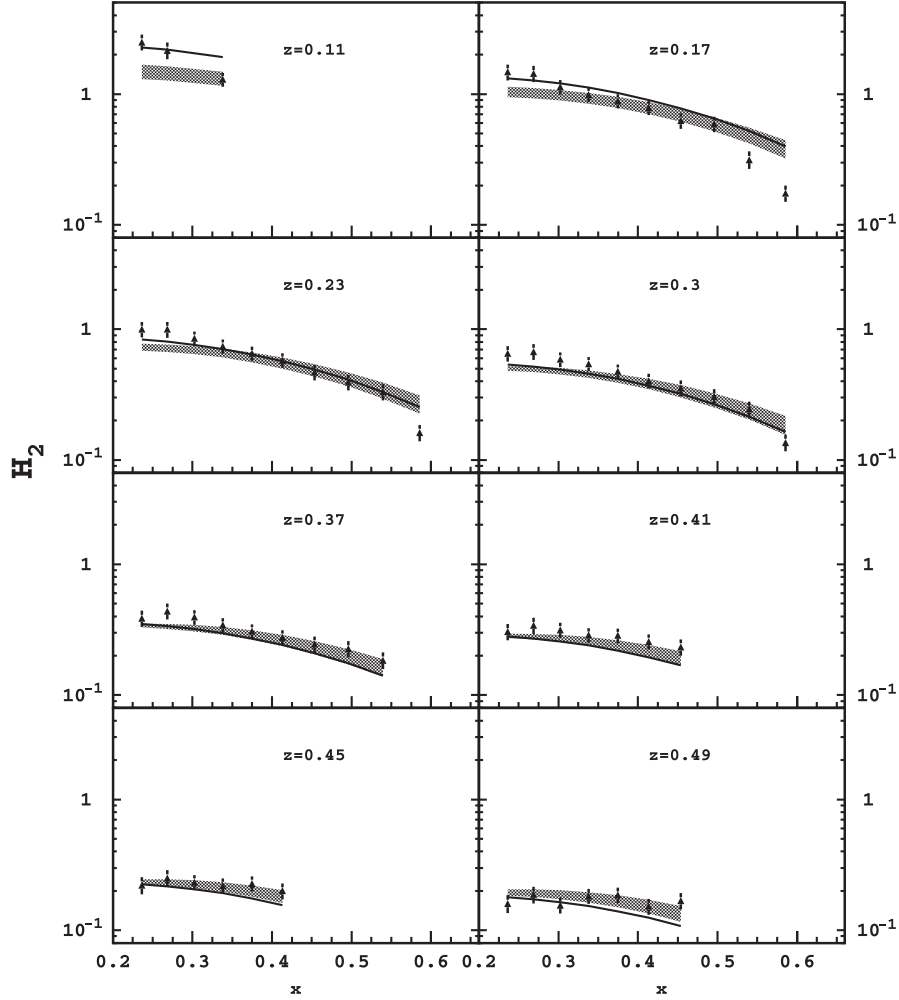


FIG. 18. Same as Fig. 17 except with H_2 plotted as a function of x rather than z .

$$H_2(x, z, Q^2) = \sum_i e_i^2 x [f_i(x, Q^2) D_i^h(z, Q^2) A(\theta_{\gamma h} = 0) + (1-x) M_i^h(x, z, Q^2) A(\theta_{\gamma h} = \pi)], \quad (29)$$

where $D_i^h(z)$ is the fragmentation function, $M_i^h(x, z)$ is the fracture function [1] and $A(\theta_{\gamma h})$ is the angular distribution of the observed hadron [66]. The fracture function $M_i^h(x, z)$ gives the combined probability of striking a parton of flavor i at x and producing a hadron h at z from the proton remnant. This function obeys the pQCD evolution equations [1,66] similar to those for $f_i(x)$ and $D_i^h(z)$. The factorization of the hard photon-parton scattering and a soft part described by $M_i^h(x, z)$ has been proved in Refs. [3,4].

Because the agreement between pQCD calculations and our data, shown in Fig. 17, was rather poor we could explore only qualitative behavior of the structure functions to search for the target fragmentation contribution.

To estimate target fragmentation we used two alternative sets of variables: 1) z and t , where the squared 4-

momentum transfer t provides added information on the direction of p_{\parallel} ; and 2) x_F and p_T^2 , which included the sign of the longitudinal hadron momentum in the center-of-momentum (CM) frame through Feynman x_F .

Target fragmentation is expected to appear at small z , where hadrons are kinematically allowed in the direction opposite to that of the virtual photon. In analogy with vector meson photoproduction measurements, a contribution from target fragmentation may come from u -channel exchange [67] by a particle or a set of particles (see Fig. 22). In this case the cross section would be proportional to the structure function of the exchanged particle (e.g. a neutron) or set of particles [68]. In this case one would expect a peak at $|t| = |t|_{\max}$, in addition to the dominant peak at $|t| = |t|_{\min}$ due to Regge exchange in the t -channel. This u -channel production can be called the ‘‘leading-particle’’ contribution in the target fragmentation region because the produced hadron carries almost all of the spectator momentum. However, the measured t -distribution shown in Fig. 23 displays the exponential behavior expected in Regge theory but does not show any

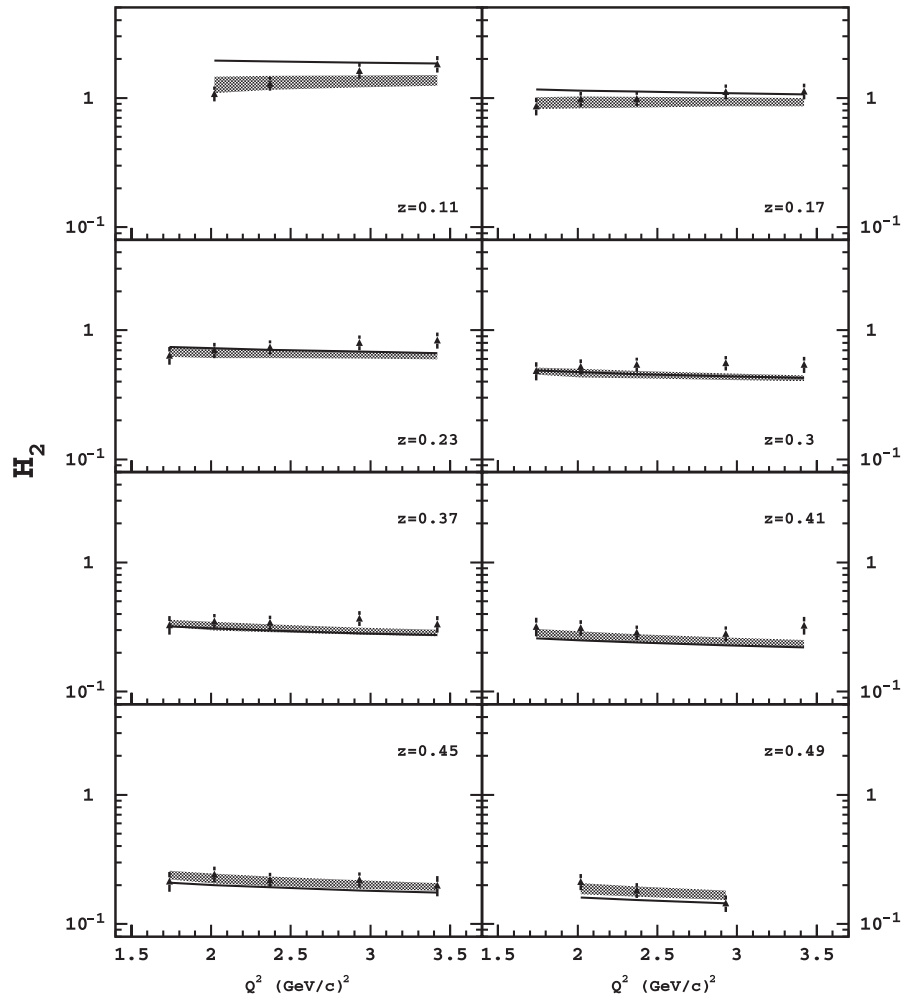


FIG. 19. Same as Fig. 17 except with H_2 plotted as a function of Q^2 rather than z at $x = 0.33$.

evidence of the second peak at $|t| = |t|_{\max}$. In Fig. 23 the solid line shows an expected u -channel exchange contribution assumed to be 1% of the t -channel term. As one can see this assumption is not supported by the data. This observation is in agreement with a known phenomenological rule that a particle not present in the initial state cannot be the leading particle in a target jet [69].

Another contribution may come from soft fragmentation of the spectator diquark. One can naively define all hadrons produced in the direction of the struck quark to be in the current fragmentation region, whereas those produced in the direction of the spectator diquark to be in the target fragmentation region. Since this definition is clearly frame-dependent, in the following we will use the CM frame.

Figure 24 shows the data for four p_T bins as a function of x_F . They exhibit a wide distribution centered at $x_F \approx 0$, which corresponds to the center of momentum. Such behavior is in good agreement with that observed in semi-inclusive π^+ production by a muon beam at much higher energies [70]. According to our definition, all hadrons at

$x_F > 0$ come from current fragmentation, while those at $x_F < 0$ come from target fragmentation.

In the CM frame, z mixes backward-angle production with the production of low-momentum forward-going hadrons [66]. In Fig. 24 the standard LO pQCD calculations are combined with a Gaussian p_T -distribution (Eq. (7)), plotted versus x_F , and compared with the data. The theory describes approximately the $x_F > 0$ behavior beginning from the $x_F \sim 0$ peak. At negative x_F values the theoretical curve is almost constant and deviates strongly from the data. This is because at $x_F < 0$, z is close to zero and varies slowly, making $D(z)$ nearly constant. In order to distinguish target and current fragmentation, one can use a different variable [66]

$$z_G = \frac{2E_h^{\text{CM}}}{W}, \quad (30)$$

in which E_h^{CM} is hadron energy in the CM frame. This can still be interpreted as the parton momentum fraction

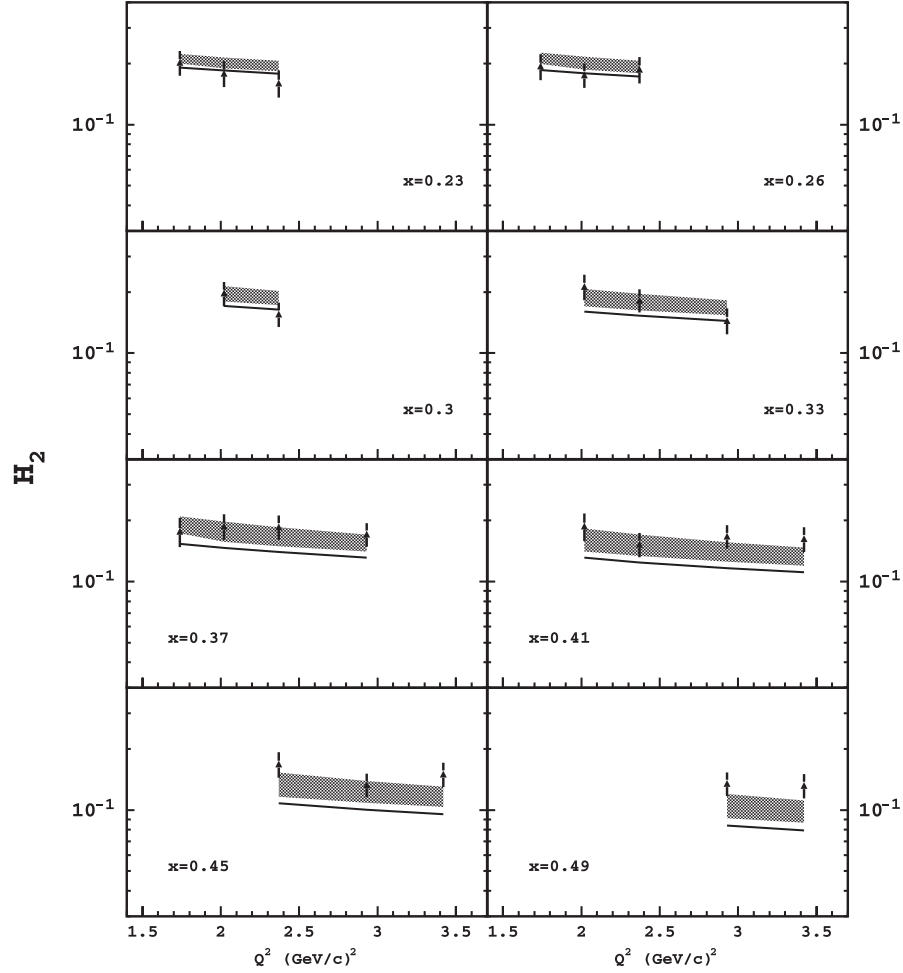


FIG. 20. Same as Fig. 17 except with H_2 plotted as a function of Q^2 rather than z at $z = 0.5$.

carried by the measured hadron, similar to that in e^+e^- collisions. By simply using the fragmentation function $D(z_G)$ in Eq. (29) for both forward and backward regions, one obtains a qualitative agreement between theoretical and experimental x_F distributions (see Fig. 25). Hence the target fragmentation term in Eq. (29) is equal to the standard “current fragmentation” contribution $(1-x)M = f(x) \otimes D(z_G)$. We speculate, therefore, that the fragmentation of the spectator diquark system may be quantitatively similar to the antiquark fragmentation (see Ref. [71]) for π^+ production. The latter mechanism is implicitly included in the fragmentation functions $D(z)$ measured in e^+e^- collisions. It is also related to the dominance of the favored u -quark fragmentation in π^+ , since the two valence u -quarks in the proton are likely to be evenly distributed between current and target fragments. This intriguing similarity allows us to describe qualitatively the semi-inclusive cross section by the standard current fragmentation $f(x) \otimes D(z_G)$ term only even in the region of backward-going π^+ s.

D. Azimuthal moments

Figures 26–28 show the p_T^2 and z -dependencies of $\mathcal{H}_3/(\mathcal{H}_2 + \epsilon\mathcal{H}_1)$ and $\mathcal{H}_4/(\mathcal{H}_2 + \epsilon\mathcal{H}_1)$. The ϕ -dependent terms are typically less than a few percent of the ϕ -independent part of the semi-inclusive cross section. The $\langle \cos 2\phi \rangle$ moments are generally compatible with zero within our systematic uncertainties, excluding the low- z and high- p_T region where they are definitely positive. The $\langle \cos \phi \rangle$ moments are more significant due to smaller systematic uncertainty and they are negative at large- p_T . By exploiting the broad kinematic coverage of CLAS, we can explore the overall trends of the data.

The $\langle \cos \phi \rangle$ term shown in Fig. 26 tends to decrease as a function of p_T and eventually becomes negative. For most of the p_T range the data are 2–3 systematic deviations below zero.

As one can see in Fig. 27, the $\langle \cos 2\phi \rangle$ term is compatible with zero point-by-point, except for the low- z and large p_T where it is positive.

The z -dependence of $\langle \cos \phi \rangle$ shown in Fig. 28 has a very different behavior at the lowest p_T and at higher p_T : at the

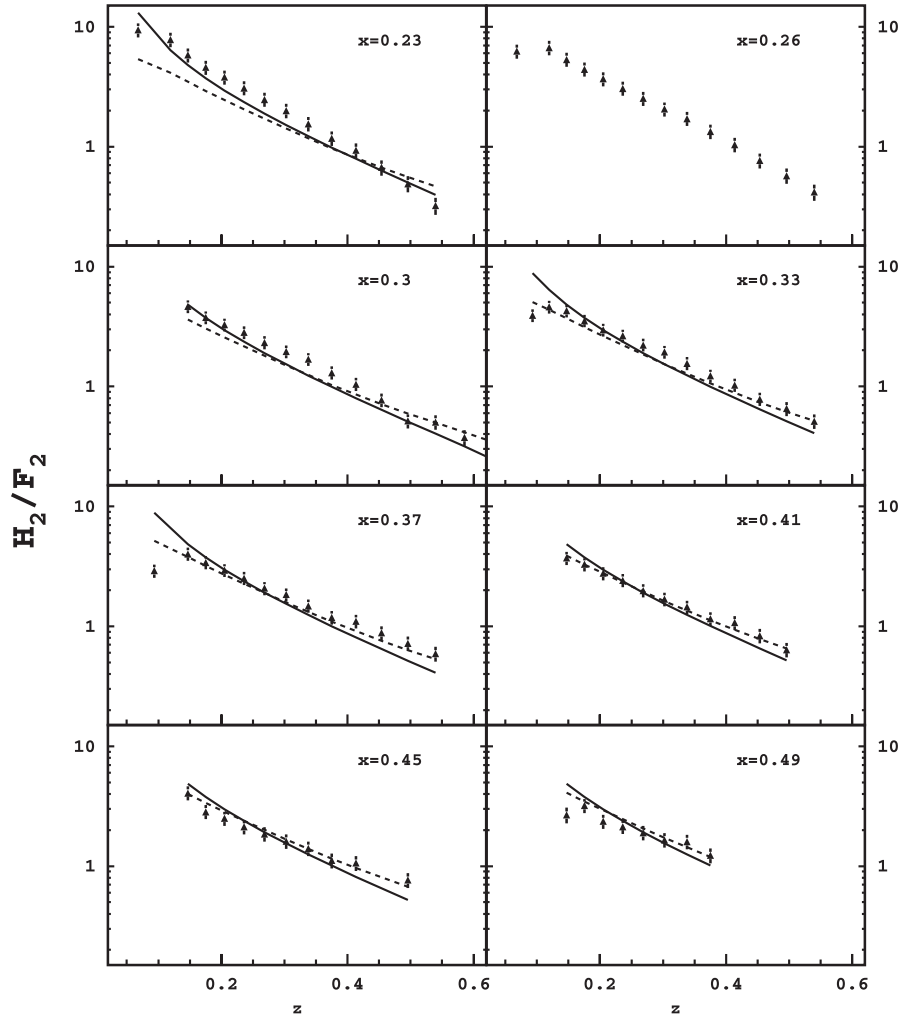


FIG. 21. Same as Fig. 17 except with H_2/F_2 , where F_2 is the inclusive structure function obtained in the same experiment. And NLO calculations are shown by the dashed line, without systematic uncertainties due to factorization and renormalization scales.

lowest p_T , $\langle \cos\phi \rangle$ is compatible with zero, whereas at higher p_T , except for the highest p_T point, $\langle \cos\phi \rangle$ rises from negative to positive values.

The $\langle \cos 2\phi \rangle$ term shown in Fig. 29 does not exhibit a clear z -dependence, except for the low- z region where positive values decreasing with z can be seen. Above that region $\langle \cos 2\phi \rangle$ is generally smaller than the systematic uncertainties.

Theoretical predictions in the $\langle \cos\phi \rangle$ are in strong disagreement with our data. Indeed the full curve of the predictions, which has a similar dependence on p_T but very different z -dependence, lies many standard deviations below the measured points over much of the kinematics. This is due to the dominant, negative Cahn effect contribution. The positive contribution of the Berger effect slightly compensates for the Cahn effect, but the Berger contribution is too small to bring the sum of the two effects in agreement with the data.

Theory predicts very small $\langle \cos 2\phi \rangle$ values partially due to cancellation between the Cahn and Berger effect con-

tributions. These predictions are generally in agreement with our data. The data points at large p_T and low z lie above the theoretical curves, this difference reaches 2–3 systematic deviations.

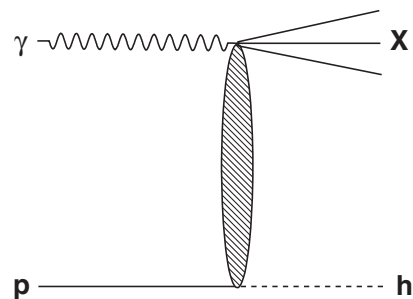


FIG. 22. Schematic representation of the leading-particle target fragmentation mechanism. The hatched blob represents the structure function of a particle or a set of particles exchanged. In case of π^+ production the first particle in the blob is the neutron.

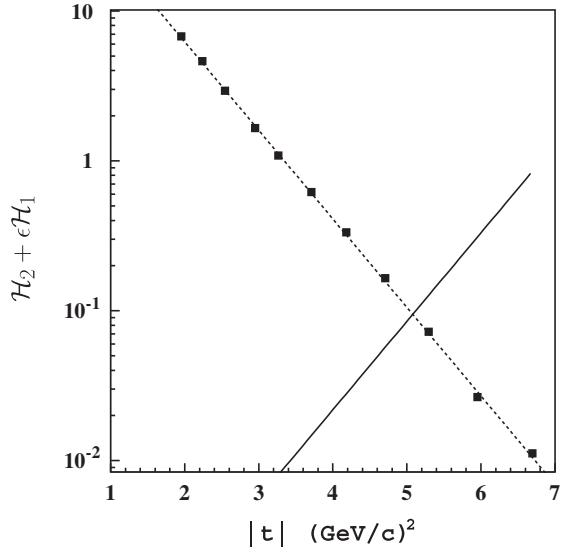


FIG. 23. The t -dependence of the ϕ -independent term $\mathcal{H}_2 + \epsilon\mathcal{H}_1$ at $Q^2 = 2$ (GeV/c) 2 , $x = 0.24$ and $z = 0.18$. The data are shown as solid squares. The curves represent the exponential fit to the data (dashes) and the expected behavior of leading-particle target fragmentation (solid), assuming it to be 1% of the t -channel exchange term. The error bars are statistical only and they are smaller than symbol size.

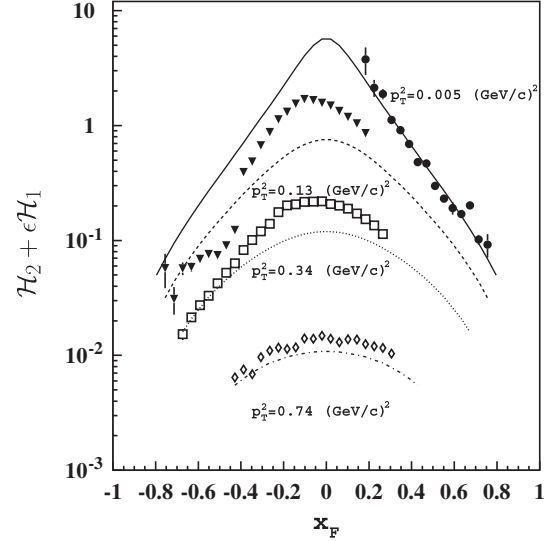


FIG. 25. Same data as in Fig. 24. The curves are the same as in Fig. 24 except for the fragmentation functions, which are evaluated at z_G rather than z .

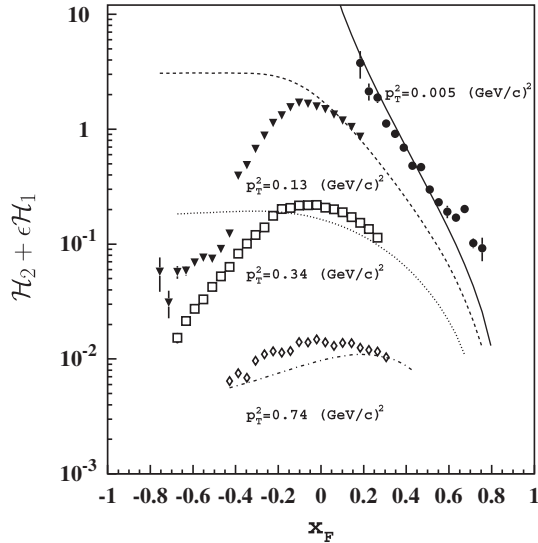


FIG. 24. The x_F -dependence of the ϕ -independent term $\mathcal{H}_2 + \epsilon\mathcal{H}_1$ at $Q^2 = 2$ (GeV/c) 2 and $x = 0.26$. The data are compared to LO pQCD calculations combined with a Gaussian p_T -dependence from Eq. (7) for $p_T^2 = 0.005$ (GeV/c) 2 (full circles and solid curve), $p_T^2 = 0.13$ (GeV/c) 2 (full triangles and dashed curve), $p_T^2 = 0.34$ (GeV/c) 2 (open squares and dotted curve), and $p_T^2 = 0.74$ (GeV/c) 2 (open diamonds and dot-dashed curve). The coverage in x_F is limited for the data by detector acceptance. The error bars are statistical only.

The averaged structure function ratios $\mathcal{H}_{3,4}/(\mathcal{H}_2 + \epsilon\mathcal{H}_1)$ shown in Figs. 26–29 are listed in Tables IX and X. We notice that the use of the weighted average technique is not strictly justified over the entire range of z and p_T . In some points, in particular, in the low- z region, the data show a clear x and/or Q^2 -dependence leading to an underestimation of the averaged statistical uncertainties. Although, the full uncertainty on the averaged data is in any case dominated by the systematic uncertainty. Not averaged data obtained from the two methods are statistically compatible.

The comparison with higher energy data from Ref. [72] shown in Fig. 30 reveals the striking difference between the two measurements of H_3 , whereas both measurements of H_4 at large and small Q^2 are compatible with zero. At large Q^2 the absolute values of the ratio H_3/H_2 reach 0.05–0.1 and seem to follow the expected $1/Q^2$ behavior. However, our data at lower Q^2 do not follow this trend having values compatible with zero. The strong suppression of H_3 at $Q^2 \approx 2$ (GeV/c) 2 with respect to the data at $Q^2 \approx 30$ –60 (GeV/c) 2 does not seem to be related to the threshold effect due to the phase space shrinkage at lower energies discussed in Ref. [73]. To account for it, the ratios of the Gaussian model integrals over the allowed kinematical region:

$$\frac{\int_{(p_T^2)_{\min}}^{(p_T^2)_{\max}} p_T \exp[-p_T^2/\langle p_T^2 \rangle] dp_T^2}{\int_{(p_T^2)_{\min}}^{(p_T^2)_{\max}} \exp[-p_T^2/\langle p_T^2 \rangle] dp_T^2} \quad (31)$$

for H_3/H_2 and

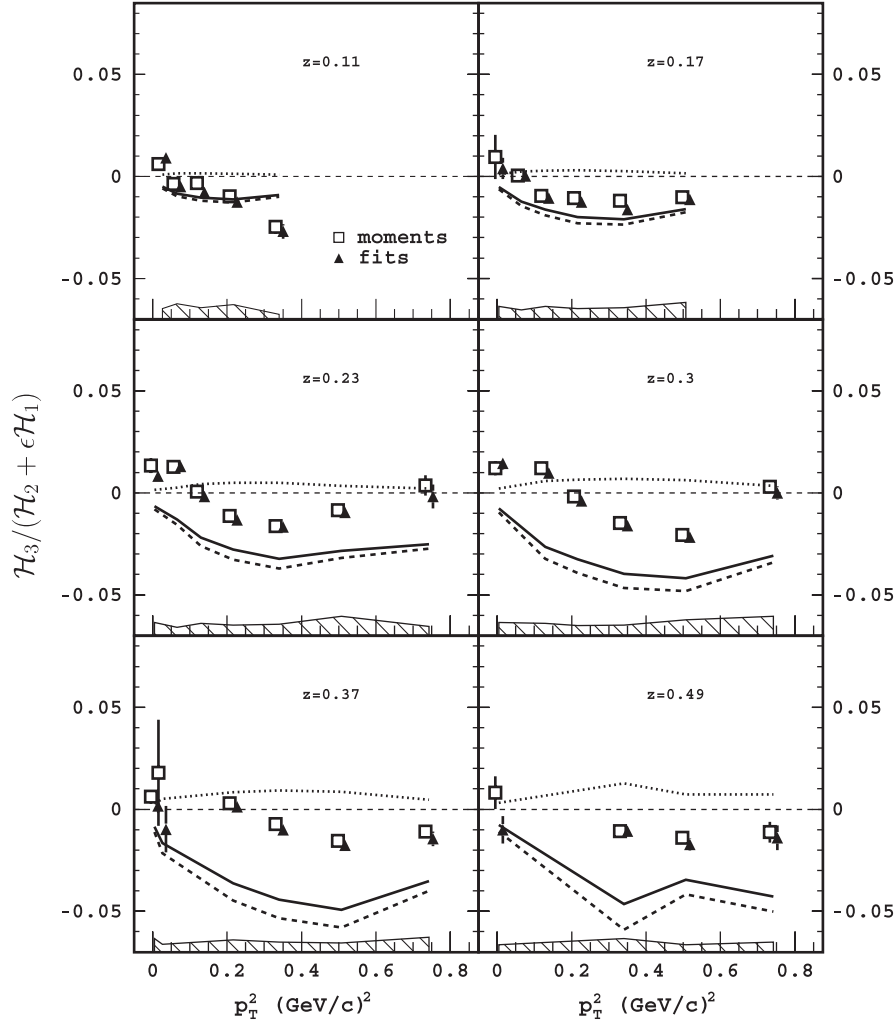


FIG. 26. The p_T^2 -dependence of $\mathcal{H}_3/(\mathcal{H}_2 + \epsilon\mathcal{H}_1)$ (open squares—moments, full triangles—fits) for different z averaged over x and Q^2 . The thick curves show theoretical predictions of the Cahn effect [31,32] (dashed), predictions of the Berger effect [41] using a convex pion wave function (dotted) and their sum (solid). The two data sets (from moments and fits extractions) are shifted equally along the x -axis in opposite directions from their central values for visibility. The hatched area show the systematic uncertainties.

$$\frac{\int_{(p_T^2)_{\min}}^{(p_T^2)_{\max}} p_T^2 \exp[-p_T^2/\langle p_T^2 \rangle] dp_T^2}{\int_{(p_T^2)_{\min}}^{(p_T^2)_{\max}} \exp[-p_T^2/\langle p_T^2 \rangle] dp_T^2} \quad (32)$$

for H_4/H_2 are included in the Cahn effect curves in Fig. 30. These corrections do not affect strongly the Cahn effect curves in the presented interval of Q^2 .

V. CONCLUSIONS

We performed a measurement of semi-inclusive π^+ electroproduction in the Q^2 range from 1.4 to 5.7 (GeV/c)² with broad coverage in all other kinematic variables. The five-fold differential cross sections allowed us to separate the contributions of different structure functions. From these data we draw the following conclusions:

- (i) The transverse momentum dependence for the ϕ -independent term $\mathcal{H}_2 + \epsilon\mathcal{H}_1$ exhibits the expected thermal Gaussian distribution.
- (ii) At large z the mean transverse momentum $\langle p_T^2 \rangle$ is found to be x and Q^2 -independent and it rises with z as expected within the naive parton model. In the low- z region, $\langle p_T^2 \rangle$ is altered by the limited phase space.
- (iii) The comparison of the measured structure function H_2 to the current fragmentation LO and NLO pQCD calculations shows that the difference between the data and calculations reaches 20% at the low- x limit of the $z < 0.4$ region, which is compatible with systematic uncertainties in the calculations due to higher-order corrections and the favored fragmentation assumption.
- (iv) The separation of the current and soft target fragmentation processes in the CM frame shows a sym-

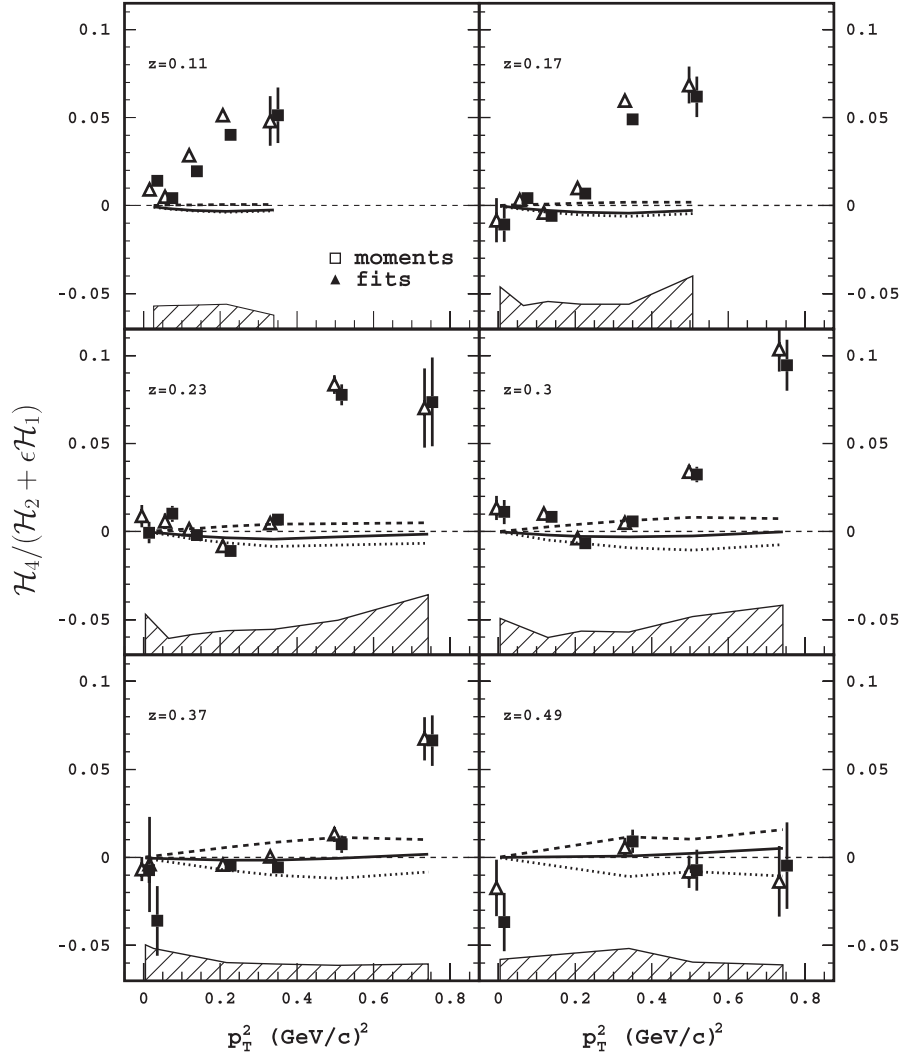


FIG. 27. Same as Fig. 26 except for $\mathcal{H}_4/(\mathcal{H}_2 + \epsilon\mathcal{H}_1)$ arising from the $\langle \cos 2\phi \rangle$ moment (open triangles—moments, full squares—fits).

metry about $x_F = 0$, which suggests the presence of an intriguing numerical equality between the fragmentation of the spectator diquark in the target region of SIDIS and the fragmentation of the antiquark in e^+e^- collisions.

- (v) The precision of the data does not allow us to obtain information about the contribution of the Boer-Mulders function, which is expected to be smaller than our estimated systematic uncertainties [34,74].
- (vi) The \mathcal{H}_4 structure function is compatible with zero within our precision, except for the low- z region where it is positive. The \mathcal{H}_3 structure function appears to be somewhat better determined than \mathcal{H}_4 and is in strong disagreement with the predictions of the Cahn effect. Inclusion of the Berger effect does not change significantly the disagreement in \mathcal{H}_3 .

- (vii) H_3 structure function at $Q^2 \approx 2(\text{GeV}/c)^2$ found to be strongly suppressed with respect to the data at $Q^2 \approx 30\text{--}60 (\text{GeV}/c)^2$. This suppression does not seem to be related to the phase space shrinkage at our energies.

The data tables can be found in the CLAS physics database [75] and in sources of the electronic preprint [76].

ACKNOWLEDGMENTS

We thank P. Mulders and E. Di Salvo for helpful discussions. We also would like to acknowledge the outstanding efforts of the staff of the Accelerator and the Physics Divisions at JLab that made this experiment possible. This work was supported in part by the Istituto Nazionale di Fisica Nucleare, the French Centre National de la Recherche Scientifique, the French Commissariat à l'Énergie Atomique, the U.S. Department of Energy, the

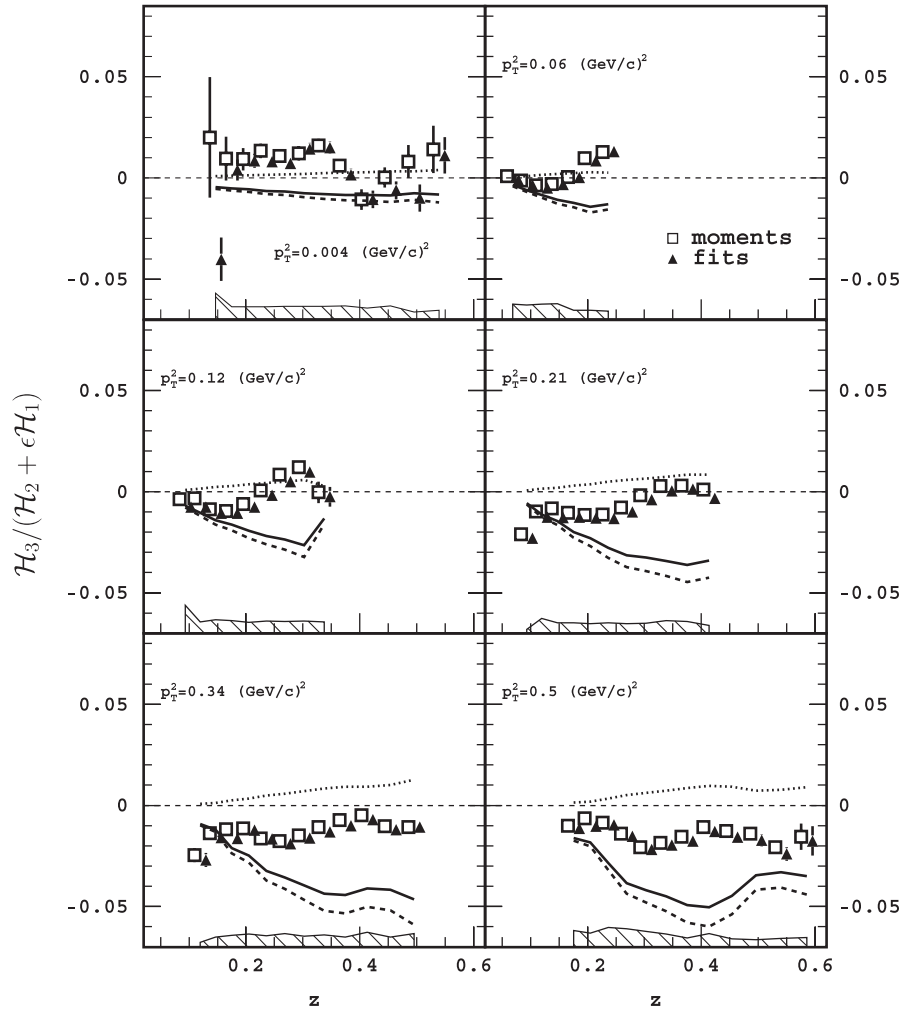


FIG. 28. Same as Fig. 26 except with $\mathcal{H}_3/(\mathcal{H}_2 + \epsilon\mathcal{H}_1)$ plotted as a function of z rather than p_T^2 .

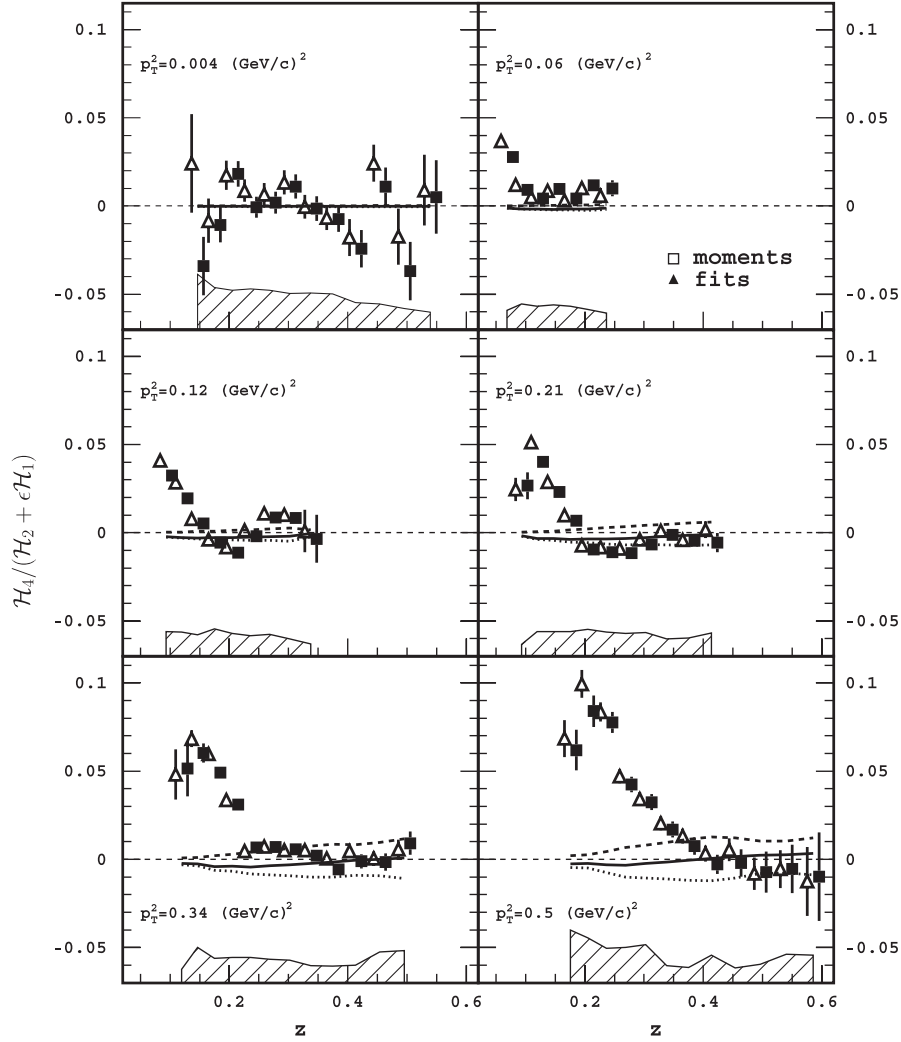


FIG. 29. Same as Fig. 27 except with $\mathcal{H}_4/(\mathcal{H}_2 + \epsilon\mathcal{H}_1)$ plotted as a function of z rather than p_T^2 .

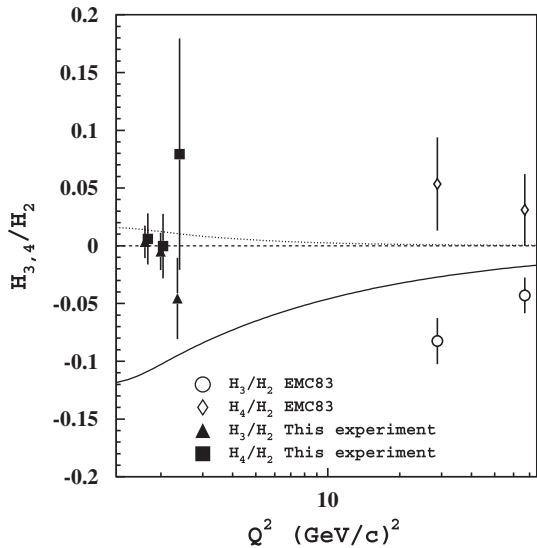


FIG. 30. The Q^2 -dependence of H_3/H_2 (full triangles) and H_4/H_2 (full squares) extracted using $R = 0.12$ from the present data in comparison with measurements from Ref. [72] (open circles— H_3/H_2 , diamonds— H_4/H_2) at $x = 0.24$. Both data sets are integrated over $z > 0.2$ and $p_T > 0.2$ GeV/c ($\langle z \rangle = 0.27$, $\langle p_T^2 \rangle = 0.22$ (GeV/c) 2). The curves show predictions of the Cahn effect [31,32] for H_4/H_2 (dotted) and H_3/H_2 (solid), corrected for the phase space shrinkage using Eqs. (32) and (31), respectively. The statistical and systematic uncertainties are combined in quadrature.

TABLE V. H_2 structure function with its statistical and systematic uncertainties.

z	H_2	stat.err.	sys.err.	z	H_2	stat.err.	sys.err.	z	H_2	stat.err.	sys.err.	z	H_2	stat.err.	sys.err.
$Q^2 = 1.49 \text{ (GeV}/c^2)^2, x = 0.15$				0.37	0.418	0.003	0.058	0.41	0.321	0.015	0.051	0.50	0.179	0.003	0.026
0.07	3.746	0.038	0.548	0.41	0.324	0.003	0.046	0.45	0.215	0.014	0.034	0.54	0.134	0.004	0.020
0.09	3.897	0.022	0.605	0.45	0.232	0.003	0.033	$Q^2 = 1.74 \text{ (GeV}/c^2)^2, x = 0.37$				0.59	0.087	0.003	0.013
0.12	2.957	0.018	0.451	0.50	0.176	0.003	0.026	0.18	0.724	0.025	0.109	0.68	0.032	0.003	0.006
0.15	2.195	0.015	0.328	0.54	0.134	0.004	0.021	0.21	0.631	0.048	0.096	$Q^2 = 2.02 \text{ (GeV}/c^2)^2, x = 0.27$			
0.18	1.735	0.012	0.256	0.59	0.099	0.003	0.016	0.24	0.490	0.021	0.074	0.09	1.544	0.011	0.209
0.21	1.359	0.011	0.200	$Q^2 = 1.74 \text{ (GeV}/c^2)^2, x = 0.24$				0.27	0.404	0.018	0.061	0.12	1.633	0.006	0.221
0.24	1.084	0.010	0.159	0.09	1.527	0.012	0.209	0.30	0.431	0.026	0.067	0.15	1.413	0.005	0.191
0.27	0.861	0.009	0.126	0.12	1.660	0.008	0.228	0.34	0.296	0.016	0.046	0.18	1.163	0.004	0.154
0.30	0.661	0.008	0.097	0.15	1.444	0.007	0.197	0.37	0.280	0.014	0.044	0.21	1.009	0.004	0.133
0.34	0.499	0.008	0.073	0.18	1.215	0.006	0.163	0.41	0.269	0.013	0.042	0.24	0.846	0.004	0.111
0.37	0.412	0.007	0.061	0.21	1.049	0.005	0.140	0.45	0.205	0.010	0.032	0.27	0.716	0.003	0.093
0.41	0.302	0.007	0.046	0.24	0.878	0.005	0.116	0.50	0.177	0.009	0.028	0.30	0.612	0.003	0.079
0.45	0.238	0.007	0.037	0.27	0.749	0.005	0.098	$Q^2 = 1.74 \text{ (GeV}/c^2)^2, x = 0.41$				0.34	0.503	0.004	0.065
0.50	0.182	0.006	0.029	0.30	0.621	0.005	0.081	0.21	0.414	0.031	0.069	0.37	0.412	0.004	0.053
0.63	0.099	0.008	0.018	0.34	0.535	0.005	0.070	0.24	0.342	0.021	0.057	0.41	0.323	0.004	0.042
$Q^2 = 1.49 \text{ (GeV}/c^2)^2, x = 0.18$				0.37	0.435	0.005	0.057	0.27	0.354	0.025	0.060	0.45	0.250	0.004	0.033
0.12	2.374	0.013	0.334	0.41	0.339	0.006	0.045	0.30	0.391	0.023	0.066	0.50	0.176	0.005	0.024
0.15	1.896	0.012	0.261	0.45	0.252	0.005	0.033	0.34	0.310	0.017	0.053	0.54	0.174	0.005	0.024
0.18	1.574	0.010	0.213	0.50	0.203	0.005	0.028	0.37	0.210	0.013	0.036	0.59	0.121	0.003	0.017
0.21	1.279	0.009	0.172	0.54	0.131	0.006	0.019	0.41	0.216	0.014	0.037	$Q^2 = 2.02 \text{ (GeV}/c^2)^2, x = 0.30$			
0.24	1.074	0.009	0.144	0.59	0.132	0.006	0.019	$Q^2 = 1.74 \text{ (GeV}/c^2)^2, x = 0.45$				0.09	1.062	0.015	0.136
0.27	0.847	0.008	0.113	$Q^2 = 1.74 \text{ (GeV}/c^2)^2, x = 0.27$				0.27	0.294	0.028	0.044	0.12	1.389	0.007	0.178
0.30	0.724	0.008	0.096	0.09	1.133	0.024	0.153	0.30	0.301	0.040	0.045	0.15	1.255	0.006	0.162
0.34	0.569	0.007	0.076	0.12	1.394	0.011	0.188	0.34	0.232	0.021	0.035	0.18	1.057	0.006	0.136
0.37	0.437	0.007	0.058	0.18	1.126	0.010	0.153	0.41	0.172	0.019	0.026	0.21	0.899	0.005	0.116
0.41	0.383	0.008	0.052	0.21	0.959	0.008	0.130	$Q^2 = 2.02 \text{ (GeV}/c^2)^2, x = 0.21$				0.24	0.798	0.005	0.103
0.45	0.290	0.008	0.040	0.24	0.836	0.007	0.114	0.09	3.226	0.011	0.467	0.27	0.673	0.004	0.087
0.50	0.204	0.006	0.029	0.27	0.731	0.007	0.099	0.12	2.519	0.009	0.361	0.30	0.578	0.004	0.075
0.54	0.128	0.008	0.019	0.30	0.613	0.007	0.083	0.15	1.901	0.008	0.266	0.34	0.454	0.004	0.059
0.59	0.143	0.010	0.022	0.34	0.490	0.007	0.067	0.18	1.513	0.006	0.209	0.37	0.377	0.004	0.050
0.07	3.353	0.019	0.457	0.37	0.397	0.006	0.055	0.21	1.232	0.006	0.170	0.41	0.311	0.004	0.041
0.12	2.714	0.008	0.387	0.41	0.324	0.007	0.045	0.24	0.997	0.005	0.137	0.45	0.238	0.004	0.032
0.15	2.013	0.007	0.281	0.45	0.240	0.008	0.034	0.27	0.790	0.005	0.108	0.50	0.198	0.004	0.027
0.18	1.587	0.006	0.219	0.50	0.194	0.007	0.028	0.30	0.654	0.005	0.090	0.54	0.164	0.004	0.023
0.21	1.294	0.005	0.178	0.54	0.168	0.006	0.025	0.34	0.513	0.005	0.070	0.59	0.142	0.005	0.020
0.24	1.019	0.005	0.140	0.59	0.134	0.007	0.020	0.37	0.401	0.004	0.056	0.63	0.119	0.005	0.018
0.27	0.812	0.004	0.111	$Q^2 = 1.74 \text{ (GeV}/c^2)^2, x = 0.30$				0.41	0.297	0.004	0.042	$Q^2 = 2.02 \text{ (GeV}/c^2)^2, x = 0.34$			
0.30	0.644	0.004	0.088	0.15	1.123	0.015	0.164	0.45	0.228	0.004	0.033	0.12	1.084	0.018	0.143
0.34	0.503	0.004	0.069	0.18	1.011	0.013	0.147	0.50	0.171	0.004	0.026	0.15	1.128	0.009	0.150
0.37	0.389	0.004	0.054	0.21	0.878	0.014	0.128	0.54	0.122	0.005	0.019	0.18	0.980	0.007	0.130
0.41	0.302	0.003	0.043	0.24	0.726	0.011	0.106	0.59	0.097	0.005	0.015	0.21	0.897	0.007	0.119
0.45	0.220	0.003	0.032	0.27	0.608	0.009	0.089	0.63	0.071	0.004	0.013	0.24	0.702	0.006	0.093
0.50	0.176	0.003	0.027	0.30	0.535	0.009	0.078	$Q^2 = 2.02 \text{ (GeV}/c^2)^2, x = 0.24$				0.27	0.595	0.005	0.079
0.54	0.139	0.004	0.022	0.34	0.434	0.009	0.064	0.07	1.683	0.010	0.224	0.30	0.524	0.005	0.070
0.59	0.127	0.005	0.020	0.37	0.356	0.008	0.053	0.12	2.002	0.005	0.281	0.34	0.412	0.004	0.055
0.63	0.083	0.004	0.015	0.41	0.308	0.008	0.046	0.15	1.617	0.004	0.223	0.37	0.352	0.004	0.048
$Q^2 = 1.74 \text{ (GeV}/c^2)^2, x = 0.21$				0.45	0.258	0.007	0.039	0.18	1.326	0.004	0.180	0.41	0.314	0.005	0.043
0.12	2.106	0.006	0.306	$Q^2 = 1.74 \text{ (GeV}/c^2)^2, x = 0.34$				0.21	1.115	0.003	0.151	0.45	0.244	0.004	0.034
0.15	1.717	0.005	0.244	0.18	0.867	0.018	0.133	0.24	0.915	0.003	0.123	0.50	0.213	0.006	0.030
0.18	1.383	0.004	0.194	0.21	0.788	0.016	0.121	0.27	0.774	0.003	0.103	0.54	0.165	0.006	0.024
0.21	1.155	0.004	0.162	0.24	0.640	0.018	0.099	0.30	0.632	0.003	0.084	$Q^2 = 2.02 \text{ (GeV}/c^2)^2, x = 0.37$			
0.24	0.949	0.004	0.132	0.27	0.569	0.012	0.088	0.34	0.514	0.003	0.069	0.15	0.950	0.010	0.128
0.27	0.788	0.003	0.109	0.30	0.487	0.015	0.076	0.37	0.410	0.003	0.055	0.18	0.861	0.008	0.115
0.30	0.644	0.003	0.089	0.34	0.363	0.010	0.056	0.41	0.312	0.003	0.043	0.21	0.784	0.008	0.105
0.34	0.518	0.003	0.072	0.37	0.330	0.014	0.053	0.45	0.237	0.003	0.033	0.24	0.608	0.007	0.082
0.27	0.528	0.005	0.072	0.54	0.105	0.006	0.016	0.34	0.384	0.004	0.049	0.15	1.645	0.008	0.230
0.30	0.488	0.006	0.066	$Q^2 = 2.37 \text{ (GeV}/c^2)^2, x = 0.27$				0.37	0.308	0.004	0.040	0.18	1.345	0.006	0.186

TABLE VI. Continued from Table V.

z	H_2	stat.err.	sys.err.	z	H_2	stat.err.	sys.err.	z	H_2	stat.err.	sys.err.	z	H_2	stat.err.	sys.err.	
0.34	0.369	0.005	0.050	0.07	2.047	0.014	0.280	0.41	0.286	0.004	0.037	0.21	1.113	0.006	0.153	
0.37	0.320	0.005	0.044	0.12	2.162	0.006	0.311	0.45	0.228	0.004	0.030	0.24	0.926	0.006	0.127	
0.41	0.300	0.006	0.042	0.15	1.730	0.005	0.244	0.50	0.187	0.005	0.025	0.27	0.761	0.005	0.104	
0.45	0.214	0.005	0.030	0.18	1.437	0.005	0.200	0.54	0.153	0.005	0.021	0.30	0.621	0.005	0.085	
0.50	0.188	0.005	0.027	0.21	1.196	0.004	0.166	$Q^2 = 2.37 \text{ (GeV}/c)^2, x = 0.41$				0.34	0.505	0.006	0.069	
$Q^2 = 2.02 \text{ (GeV}/c)^2, x = 0.41$				0.24	0.998	0.004	0.138	0.15	0.895	0.008	0.113	0.37	0.388	0.005	0.054	
0.18	0.700	0.012	0.102	0.27	0.824	0.004	0.113	0.18	0.789	0.006	0.099	0.41	0.339	0.007	0.048	
0.21	0.639	0.008	0.094	0.30	0.675	0.004	0.093	0.21	0.663	0.007	0.084	0.45	0.224	0.005	0.032	
0.24	0.495	0.009	0.073	0.34	0.562	0.004	0.077	0.24	0.580	0.005	0.073	$Q^2 = 2.93 \text{ (GeV}/c)^2, x = 0.34$				
0.27	0.449	0.007	0.066	0.37	0.440	0.004	0.061	0.27	0.477	0.004	0.061	0.07	1.469	0.016	0.191	
0.30	0.420	0.007	0.063	0.41	0.341	0.004	0.048	0.30	0.404	0.004	0.052	0.09	1.926	0.007	0.268	
0.34	0.359	0.006	0.054	0.45	0.251	0.004	0.036	0.34	0.347	0.005	0.045	0.12	1.629	0.006	0.225	
0.37	0.293	0.005	0.045	0.50	0.188	0.004	0.028	0.37	0.277	0.004	0.036	0.15	1.378	0.005	0.187	
0.41	0.256	0.005	0.039	0.54	0.137	0.004	0.021	0.41	0.257	0.005	0.034	0.18	1.124	0.004	0.150	
0.45	0.216	0.004	0.033	0.59	0.101	0.004	0.016	0.45	0.200	0.005	0.027	0.21	0.943	0.004	0.125	
0.50	0.188	0.004	0.029	0.68	0.081	0.020	0.016	0.50	0.153	0.003	0.021	0.24	0.804	0.004	0.106	
0.54	0.147	0.004	0.023	$Q^2 = 2.37 \text{ (GeV}/c)^2, x = 0.30$				$Q^2 = 2.37 \text{ (GeV}/c)^2, x = 0.45$				0.27	0.672	0.004	0.088	
$Q^2 = 2.02 \text{ (GeV}/c)^2, x = 0.45$				0.15	1.401	0.005	0.185	0.15	0.898	0.012	0.120	0.30	0.560	0.004	0.073	
0.18	0.721	0.011	0.116	0.18	1.134	0.004	0.147	0.18	0.628	0.009	0.084	0.34	0.484	0.004	0.063	
0.21	0.489	0.009	0.079	0.21	0.989	0.004	0.128	0.21	0.553	0.006	0.074	0.37	0.370	0.004	0.049	
0.24	0.392	0.006	0.063	0.24	0.852	0.004	0.109	0.24	0.469	0.006	0.063	0.41	0.283	0.005	0.038	
0.27	0.368	0.007	0.060	0.27	0.704	0.004	0.090	0.27	0.410	0.006	0.056	0.45	0.221	0.004	0.030	
0.30	0.348	0.006	0.057	0.30	0.590	0.003	0.075	0.30	0.357	0.005	0.049	0.50	0.145	0.005	0.021	
0.34	0.295	0.006	0.049	0.34	0.511	0.004	0.065	0.34	0.309	0.005	0.043	0.54	0.110	0.004	0.016	
0.37	0.247	0.005	0.041	0.37	0.395	0.004	0.050	0.37	0.246	0.004	0.035	$Q^2 = 2.93 \text{ (GeV}/c)^2, x = 0.37$				
0.41	0.226	0.005	0.037	0.41	0.316	0.004	0.041	0.41	0.234	0.004	0.033	0.09	1.333	0.013	0.174	
0.45	0.188	0.006	0.031	0.45	0.233	0.004	0.030	0.50	0.168	0.003	0.024	0.12	1.282	0.006	0.168	
$Q^2 = 2.02 \text{ (GeV}/c)^2, x = 0.50$				0.50	0.156	0.004	0.021	$Q^2 = 2.37 \text{ (GeV}/c)^2, x = 0.50$				0.15	1.138	0.006	0.149	
0.21	0.519	0.011	0.076	0.54	0.152	0.004	0.021	0.15	0.492	0.034	0.065	0.18	0.948	0.005	0.122	
0.24	0.357	0.008	0.053	0.59	0.115	0.005	0.016	0.18	0.590	0.007	0.078	0.21	0.785	0.004	0.100	
0.27	0.289	0.010	0.043	0.63	0.095	0.006	0.014	0.21	0.435	0.007	0.059	0.24	0.711	0.004	0.090	
0.30	0.300	0.008	0.045	$Q^2 = 2.37 \text{ (GeV}/c)^2, x = 0.34$				0.24	0.394	0.005	0.053	0.27	0.609	0.004	0.077	
0.34	0.246	0.006	0.037	0.09	1.094	0.013	0.132	0.27	0.350	0.005	0.048	0.30	0.505	0.005	0.063	
0.37	0.197	0.006	0.030	0.12	1.295	0.006	0.157	0.30	0.305	0.005	0.042	0.34	0.427	0.004	0.054	
0.41	0.181	0.007	0.027	0.15	1.197	0.006	0.146	0.34	0.295	0.005	0.041	0.37	0.316	0.004	0.040	
$Q^2 = 2.02 \text{ (GeV}/c)^2 \text{ (GeV}/c)^2, x=0.54$				0.18	0.990	0.005	0.120	0.37	0.226	0.004	0.032	0.41	0.250	0.004	0.032	
0.18	0.162	0.015	0.026	0.21	0.832	0.004	0.101	$Q^2 = 2.37 \text{ (GeV}/c)^2, x = 0.54$				0.45	0.253	0.005	0.033	
0.21	0.207	0.007	0.034	0.24	0.742	0.004	0.090	0.18	0.316	0.024	0.042	0.50	0.171	0.004	0.023	
0.24	0.175	0.009	0.029	0.27	0.622	0.004	0.076	0.21	0.369	0.006	0.049	0.54	0.172	0.005	0.024	
0.27	0.176	0.006	0.029	0.30	0.544	0.005	0.067	0.24	0.332	0.014	0.045	0.59	0.117	0.005	0.016	
$Q^2 = 2.37 \text{ (GeV}/c)^2, x = 0.24$				0.34	0.437	0.004	0.054	0.27	0.297	0.009	0.041	$Q^2 = 2.93 \text{ (GeV}/c)^2, x = 0.41$				
0.07	3.085	0.030	0.419	0.37	0.343	0.004	0.043	0.30	0.246	0.005	0.033	0.12	1.089	0.007	0.128	
0.12	2.502	0.014	0.354	0.41	0.288	0.004	0.036	0.34	0.229	0.005	0.031	0.15	0.961	0.006	0.114	
0.15	1.860	0.012	0.258	0.45	0.220	0.003	0.028	0.37	0.185	0.005	0.026	0.18	0.795	0.007	0.094	
0.18	1.477	0.010	0.202	0.50	0.182	0.004	0.024	$Q^2 = 2.37 \text{ (GeV}/c)^2, x = 0.59$				0.21	0.668	0.005	0.079	
0.21	1.224	0.009	0.168	0.54	0.143	0.003	0.019	0.18	0.175	0.007	0.024	0.24	0.600	0.005	0.072	
0.24	1.000	0.008	0.136	$Q^2 = 2.37 \text{ (GeV}/c)^2, x = 0.37$				0.21	0.180	0.004	0.025	0.27	0.544	0.005	0.065	
0.27	0.805	0.008	0.109	0.09	0.755	0.026	0.093	0.24	0.162	0.004	0.023	0.30	0.418	0.004	0.051	
0.30	0.653	0.008	0.089	0.15	1.044	0.008	0.130	0.27	0.142	0.005	0.020	0.34	0.367	0.004	0.045	
0.34	0.509	0.008	0.070	0.18	0.886	0.007	0.110	0.30	0.136	0.005	0.019	0.37	0.277	0.004	0.034	
0.37	0.387	0.007	0.054	0.21	0.762	0.006	0.095	0.34	0.129	0.003	0.018	0.41	0.235	0.004	0.029	
0.41	0.306	0.006	0.043	0.24	0.653	0.005	0.082	$Q^2 = 2.93 \text{ (GeV}/c)^2, x = 0.30$				0.45	0.240	0.006	0.031	
0.45	0.221	0.006	0.032	0.27	0.540	0.004	0.068	0.09	2.623	0.010	0.377	0.50	0.167	0.005	0.022	
0.50	0.160	0.006	0.024	0.30	0.477	0.005	0.061	0.12	2.089	0.008	0.297	$Q^2 = 2.93 \text{ (GeV}/c)^2, x = 0.45$				
0.09	0.522	0.024	0.063	0.24	0.840	0.018	0.117	0.24	0.435	0.005	0.054	0.24	0.566	0.008	0.076	
0.12	0.940	0.010	0.113	0.27	0.655	0.016	0.091	0.27	0.383	0.004	0.048	0.27	0.457	0.008	0.061	
0.15	0.794	0.007	0.096	0.30	0.545	0.017	0.076	0.30	0.313	0.005	0.039	0.30	0.416	0.009	0.056	
0.18	0.738	0.007	0.089	0.34	0.445	0.017	0.062	0.34	0.259	0.004	0.032	0.34	0.329	0.009	0.044	

TABLE VII. Continued from Table V.

z	H_2	stat.err.	sys.err.	z	H_2	stat.err.	sys.err.	z	H_2	stat.err.	sys.err.	z	H_2	stat.err.	sys.err.	
0.21	0.560	0.007	0.068	0.37	0.335	0.015	0.047	0.37	0.247	0.006	0.032	0.37	0.231	0.011	0.031	
0.24	0.509	0.005	0.062	0.41	0.328	0.022	0.047	0.41	0.184	0.005	0.024	0.41	0.206	0.011	0.028	
0.27	0.461	0.005	0.057	0.45	0.199	0.020	0.029	0.45	0.182	0.005	0.024	0.45	0.138	0.013	0.019	
0.30	0.342	0.004	0.042	$Q^2 = 3.42 \text{ (GeV}/c)^2, x = 0.37$				0.50	0.132	0.004	0.018	$Q^2 = 4.10 \text{ (GeV}/c)^2, x = 0.50$				
0.34	0.300	0.004	0.037	0.09	1.847	0.011	0.261	$Q^2 = 3.42 \text{ (GeV}/c)^2, x = 0.54$				0.09	0.950	0.010	0.134	
0.37	0.236	0.005	0.030	0.12	1.521	0.008	0.214	0.12	0.775	0.012	0.091	0.12	0.872	0.007	0.121	
0.41	0.215	0.005	0.027	0.15	1.242	0.008	0.172	0.15	0.516	0.007	0.061	0.15	0.747	0.008	0.102	
0.45	0.213	0.005	0.028	0.18	1.033	0.006	0.141	0.18	0.466	0.006	0.055	0.18	0.609	0.006	0.082	
0.50	0.133	0.003	0.018	0.21	0.880	0.006	0.119	0.21	0.355	0.006	0.043	0.21	0.546	0.007	0.073	
0.54	0.143	0.003	0.020	0.24	0.749	0.006	0.101	0.24	0.321	0.004	0.039	0.24	0.481	0.006	0.064	
$Q^2 = 2.93 \text{ (GeV}/c)^2, x = 0.50$				0.27	0.617	0.006	0.083	0.27	0.335	0.005	0.041	0.27	0.393	0.006	0.052	
0.15	0.734	0.010	0.089	0.30	0.525	0.006	0.070	0.30	0.247	0.004	0.031	0.30	0.357	0.007	0.047	
0.18	0.619	0.007	0.075	0.34	0.442	0.006	0.059	0.34	0.206	0.004	0.026	0.34	0.276	0.006	0.037	
0.21	0.432	0.007	0.053	0.37	0.349	0.006	0.047	0.37	0.221	0.004	0.028	0.37	0.214	0.006	0.029	
0.24	0.405	0.006	0.050	0.41	0.258	0.007	0.035	0.41	0.159	0.003	0.020	0.41	0.180	0.006	0.024	
0.27	0.457	0.007	0.058	0.45	0.198	0.007	0.028	0.45	0.151	0.004	0.020	0.45	0.135	0.007	0.019	
0.30	0.306	0.005	0.039	$Q^2 = 3.42 \text{ (GeV}/c)^2, x = 0.41$				$Q^2 = 3.42 \text{ (GeV}/c)^2, x = 0.59$				$Q^2 = 4.10 \text{ (GeV}/c)^2, x = 0.54$				
0.34	0.281	0.005	0.036	0.09	1.458	0.009	0.200	0.15	0.406	0.006	0.049	0.09	0.539	0.017	0.066	
0.37	0.219	0.003	0.028	0.12	1.270	0.007	0.173	0.18	0.356	0.006	0.043	0.12	0.629	0.007	0.077	
0.41	0.195	0.003	0.025	0.15	1.025	0.007	0.137	0.21	0.291	0.007	0.036	0.15	0.571	0.007	0.070	
0.50	0.135	0.003	0.018	0.18	0.866	0.005	0.114	0.24	0.259	0.004	0.032	0.18	0.458	0.006	0.056	
$Q^2 = 2.93 \text{ (GeV}/c)^2, x = 0.54$				0.21	0.770	0.005	0.101	0.27	0.237	0.004	0.030	0.21	0.426	0.006	0.052	
0.15	0.605	0.008	0.074	0.24	0.662	0.005	0.086	0.30	0.204	0.004	0.026	0.24	0.364	0.005	0.045	
0.18	0.491	0.007	0.060	0.27	0.548	0.005	0.071	0.34	0.167	0.003	0.021	0.27	0.292	0.006	0.036	
0.21	0.327	0.006	0.040	0.30	0.474	0.006	0.061	$Q^2 = 3.42 \text{ (GeV}/c)^2, x = 0.63$				0.30	0.268	0.006	0.033	
0.24	0.322	0.005	0.040	0.34	0.382	0.005	0.049	0.15	0.193	0.007	0.024	0.34	0.233	0.005	0.029	
0.27	0.329	0.005	0.042	0.37	0.300	0.005	0.039	0.18	0.233	0.004	0.029	0.37	0.204	0.007	0.026	
0.30	0.242	0.004	0.031	0.41	0.231	0.005	0.030	0.21	0.159	0.006	0.020	0.41	0.162	0.006	0.021	
0.34	0.221	0.004	0.028	0.45	0.200	0.006	0.026	0.24	0.187	0.009	0.024	0.45	0.130	0.006	0.017	
0.37	0.203	0.003	0.026	0.50	0.163	0.006	0.022	0.27	0.181	0.007	0.023	0.50	0.110	0.004	0.015	
0.41	0.136	0.003	0.018	0.54	0.128	0.006	0.018	0.30	0.155	0.006	0.020	$Q^2 = 4.10 \text{ (GeV}/c)^2, x = 0.59$				
$Q^2 = 2.93 \text{ (GeV}/c)^2, x = 0.59$				$Q^2 = 3.42 \text{ (GeV}/c)^2, x = 0.45$				0.34	0.117	0.004	0.015	0.09	0.408	0.015	0.047	
0.18	0.396	0.006	0.052	0.09	0.982	0.009	0.118	$Q^2 = 3.42 \text{ (GeV}/c)^2, x = 0.68$				0.12	0.510	0.007	0.059	
0.21	0.280	0.005	0.037	0.12	0.978	0.007	0.117	0.15	0.083	0.004	0.010	0.15	0.427	0.008	0.050	
0.24	0.248	0.007	0.033	0.15	0.848	0.007	0.102	0.18	0.104	0.003	0.012	0.18	0.337	0.006	0.039	
0.27	0.224	0.007	0.030	0.18	0.735	0.006	0.089	0.24	0.082	0.003	0.010	0.21	0.298	0.006	0.036	
0.30	0.177	0.004	0.024	0.21	0.623	0.005	0.075	0.27	0.088	0.003	0.011	0.24	0.312	0.007	0.037	
0.34	0.162	0.005	0.022	0.24	0.534	0.005	0.065	$Q^2 = 4.10 \text{ (GeV}/c)^2, x = 0.41$				0.27	0.249	0.005	0.030	
0.37	0.149	0.005	0.020	0.27	0.478	0.005	0.058	0.09	1.718	0.049	0.259	0.30	0.229	0.005	0.028	
$Q^2 = 2.93 \text{ (GeV}/c)^2, x = 0.63$				0.30	0.382	0.005	0.047	0.12	1.406	0.039	0.209	0.34	0.176	0.004	0.022	
0.15	0.122	0.006	0.017	0.34	0.308	0.004	0.038	0.15	0.992	0.034	0.146	0.37	0.144	0.004	0.018	
0.18	0.154	0.004	0.022	0.37	0.263	0.005	0.033	0.18	0.918	0.029	0.133	0.41	0.154	0.004	0.019	
0.21	0.138	0.003	0.020	0.41	0.211	0.004	0.026	0.21	0.764	0.030	0.110	$Q^2 = 4.10 \text{ (GeV}/c)^2, x = 0.63$				
0.24	0.125	0.003	0.018	0.45	0.212	0.007	0.028	0.24	0.628	0.026	0.090	0.15	0.333	0.006	0.041	
0.27	0.150	0.005	0.022	0.50	0.150	0.006	0.020	0.30	0.383	0.024	0.055	0.18	0.264	0.006	0.032	
0.34	0.099	0.002	0.014	0.54	0.137	0.007	0.019	$Q^2 = 4.10 \text{ (GeV}/c)^2, x = 0.45$				0.21	0.218	0.005	0.027	
$Q^2 = 3.42 \text{ (GeV}/c)^2, x = 0.34$				$Q^2 = 3.42 \text{ (GeV}/c)^2, x = 0.50$				0.07	1.033	0.033	0.137	0.24	0.207	0.004	0.026	
0.07	2.260	0.064	0.312	0.09	0.542	0.008	0.066	0.09	1.245	0.013	0.177	0.27	0.168	0.004	0.022	
0.12	1.835	0.024	0.264	0.12	0.827	0.010	0.101	0.12	1.102	0.011	0.156	0.30	0.168	0.004	0.022	
0.15	1.379	0.021	0.196	0.15	0.670	0.006	0.082	0.15	0.896	0.010	0.124	0.34	0.141	0.004	0.018	
0.18	1.133	0.018	0.159	0.18	0.592	0.007	0.072	0.18	0.746	0.008	0.102	$Q^2 = 4.10 \text{ (GeV}/c)^2, x = 0.68$				
0.21	0.977	0.018	0.137	0.21	0.510	0.006	0.063	0.21	0.648	0.008	0.088	0.15	0.147	0.003	0.018	
0.18	0.131	0.003	0.016	0.09	0.599	0.012	0.081	0.15	0.318	0.008	0.042	0.30	0.108	0.004	0.014	
0.21	0.136	0.006	0.017	0.12	0.492	0.010	0.064	0.18	0.228	0.007	0.030	0.34	0.100	0.004	0.013	
0.24	0.131	0.006	0.016	0.15	0.435	0.010	0.057	0.21	0.216	0.006	0.029	$Q^2 = 4.85 \text{ (GeV}/c)^2, x = 0.74$				
$Q^2 = 4.10 \text{ (GeV}/c)^2, x = 0.74$				0.18	0.370	0.008	0.048	0.24	0.189	0.006	0.025	0.15	0.086	0.003	0.010	
0.15	0.076	0.005	0.009	0.21	0.321	0.008	0.042	0.27	0.170	0.005	0.023	0.21	0.082	0.004	0.010	
0.18	0.067	0.003	0.008	0.24	0.304	0.008	0.040	0.30	0.138	0.006	0.019	$Q^2 = 5.72 \text{ (GeV}/c)^2, x = 0.68$				

TABLE VIII. Continued from Table V.

z	H_2	stat.err.	sys.err.	z	H_2	stat.err.	sys.err.	z	H_2	stat.err.	sys.err.	z	H_2	stat.err.	sys.err.
$Q^2 = 4.85 \text{ (GeV}/c)^2, x = 0.54$				0.27	0.230	0.007	0.030	0.34	0.144	0.005	0.020	0.09	0.308	0.024	0.047
0.09	0.817	0.023	0.124	0.30	0.202	0.009	0.027	0.37	0.111	0.005	0.016	0.12	0.265	0.011	0.041
0.12	0.658	0.016	0.098	0.34	0.184	0.011	0.025	$Q^2 = 4.85 \text{ (GeV}/c)^2, x = 0.68$				0.15	0.205	0.014	0.032
0.15	0.600	0.018	0.088	0.37	0.127	0.009	0.017	0.15	0.218	0.005	0.027	0.18	0.156	0.013	0.024
0.18	0.499	0.014	0.073	0.41	0.141	0.013	0.019	0.18	0.227	0.009	0.028	0.21	0.124	0.010	0.019
0.21	0.424	0.014	0.061	$Q^2 = 4.85 \text{ (GeV}/c)^2, x = 0.63$				0.21	0.145	0.006	0.018	0.30	0.114	0.011	0.018
0.27	0.305	0.015	0.044	0.09	0.345	0.012	0.045	0.24	0.136	0.004	0.017	$Q^2 = 5.72 \text{ (GeV}/c)^2, x = 0.74$			
$Q^2 = 4.85 \text{ (GeV}/c)^2, x = 0.59$				0.12	0.350	0.006	0.046	0.27	0.129	0.004	0.017	0.15	0.127	0.008	0.019

TABLE IX. The extracted data on $\mathcal{H}_3/(\mathcal{H}_2 + \epsilon\mathcal{H}_1)$ averaged over x and Q^2 with their statistical and systematic uncertainties. The values given in brackets are obtained using the fit method.

z	$p_T^2 \text{ (GeV}/c)^2$	$\langle y \rangle$	$\langle Q^2 \rangle \text{ (GeV}/c)^2$	$\langle x \rangle$	$\mathcal{H}_3/(\mathcal{H}_2 + \epsilon\mathcal{H}_1)$	stat. uncertainty	sys. uncertainty
0.068	0.026	0.88 (0.87)	2.12 (2.22)	0.23 (0.24)	0.012 (0.012)	0.0007 (0.0007)	0.005
0.068	0.065	0.88 (0.87)	2.14 (2.19)	0.23 (0.23)	0.001 (-0.001)	0.0004 (0.0005)	0.008
0.093	0.026	0.85 (0.84)	2.14 (2.30)	0.24 (0.26)	0.009 (0.010)	0.0005 (0.0005)	0.006
0.093	0.065	0.83 (0.83)	2.27 (2.31)	0.26 (0.26)	-0.001 (-0.003)	0.0002 (0.0003)	0.007
0.093	0.129	0.87 (0.87)	2.10 (2.13)	0.22 (0.23)	-0.004 (-0.008)	0.0004 (0.0004)	0.014
0.093	0.217	0.92 (0.92)	1.85 (1.86)	0.19 (0.19)	-0.021 (-0.023)	0.0015 (0.0017)	0.002
0.119	0.026	0.84 (0.83)	2.12 (2.26)	0.24 (0.26)	0.006 (0.009)	0.0009 (0.0008)	0.005
0.119	0.065	0.81 (0.81)	2.28 (2.35)	0.27 (0.27)	-0.004 (-0.005)	0.0003 (0.0003)	0.008
0.119	0.129	0.84 (0.84)	2.23 (2.27)	0.25 (0.25)	-0.003 (-0.008)	0.0003 (0.0003)	0.006
0.119	0.217	0.88 (0.88)	2.01 (2.03)	0.21 (0.22)	-0.010 (-0.013)	0.0006 (0.0006)	0.007
0.119	0.340	0.93 (0.93)	1.66 (1.66)	0.17 (0.17)	-0.025 (-0.027)	0.0033 (0.0035)	0.002
0.147	0.005	0.61 (0.59)	2.83 (2.65)	0.42 (0.41)	0.020 (-0.040)	0.0298 (0.0107)	0.013
0.147	0.026	0.89 (0.91)	1.89 (1.99)	0.20 (0.20)	0.007 (0.012)	0.0035 (0.0013)	0.003
0.147	0.065	0.81 (0.80)	2.20 (2.32)	0.26 (0.27)	-0.003 (-0.003)	0.0004 (0.0004)	0.008
0.147	0.129	0.82 (0.82)	2.23 (2.28)	0.26 (0.26)	-0.009 (-0.011)	0.0003 (0.0004)	0.007
0.147	0.217	0.85 (0.85)	2.14 (2.18)	0.24 (0.24)	-0.008 (-0.013)	0.0004 (0.0005)	0.005
0.147	0.340	0.91 (0.91)	1.99 (2.01)	0.20 (0.20)	-0.014 (-0.016)	0.0011 (0.0013)	0.005
0.175	0.005	0.59 (0.60)	2.57 (2.55)	0.40 (0.39)	0.009 (0.004)	0.0109 (0.0052)	0.006
0.175	0.065	0.82 (0.81)	2.19 (2.31)	0.25 (0.27)	0.000 (0.000)	0.0005 (0.0005)	0.004
0.175	0.129	0.82 (0.82)	2.28 (2.34)	0.26 (0.27)	-0.010 (-0.011)	0.0004 (0.0004)	0.006
0.175	0.217	0.84 (0.84)	2.20 (2.24)	0.24 (0.25)	-0.011 (-0.013)	0.0004 (0.0005)	0.005
0.175	0.340	0.87 (0.87)	2.02 (2.04)	0.22 (0.22)	-0.012 (-0.016)	0.0007 (0.0008)	0.006
0.175	0.507	0.92 (0.92)	1.85 (1.86)	0.19 (0.19)	-0.010 (-0.011)	0.0024 (0.0026)	0.008
0.205	0.005	0.60 (0.62)	2.65 (2.68)	0.41 (0.40)	0.009 (0.008)	0.0056 (0.0035)	0.006
0.205	0.065	0.82 (0.81)	2.12 (2.23)	0.25 (0.26)	0.010 (0.008)	0.0008 (0.0007)	0.004
0.205	0.129	0.81 (0.81)	2.27 (2.34)	0.26 (0.27)	-0.006 (-0.008)	0.0004 (0.0005)	0.005
0.205	0.217	0.84 (0.83)	2.24 (2.28)	0.25 (0.26)	-0.012 (-0.013)	0.0005 (0.0005)	0.005
0.205	0.340	0.87 (0.86)	2.14 (2.17)	0.23 (0.23)	-0.011 (-0.012)	0.0007 (0.0008)	0.006
0.205	0.507	0.92 (0.92)	1.85 (1.87)	0.19 (0.19)	-0.006 (-0.010)	0.0018 (0.0020)	0.007
0.236	0.005	0.59 (0.61)	2.56 (2.61)	0.40 (0.39)	0.013 (0.008)	0.0036 (0.0027)	0.006
0.236	0.065	0.86 (0.86)	1.86 (1.87)	0.20 (0.20)	0.013 (0.013)	0.0024 (0.0020)	0.004
0.236	0.129	0.81 (0.81)	2.23 (2.32)	0.26 (0.27)	0.001 (-0.002)	0.0005 (0.0005)	0.006
0.236	0.217	0.82 (0.82)	2.23 (2.28)	0.26 (0.26)	-0.011 (-0.013)	0.0005 (0.0005)	0.005
0.236	0.340	0.84 (0.84)	2.15 (2.17)	0.24 (0.24)	-0.016 (-0.017)	0.0006 (0.0007)	0.006
0.236	0.507	0.90 (0.90)	1.97 (1.99)	0.20 (0.21)	-0.009 (-0.010)	0.0014 (0.0016)	0.010
0.236	0.743	0.93 (0.93)	1.66 (1.67)	0.17 (0.17)	0.004 (-0.002)	0.0050 (0.0058)	0.004
0.269	0.005	0.61 (0.63)	2.66 (2.67)	0.40 (0.39)	0.011 (0.007)	0.0033 (0.0027)	0.006
0.269	0.129	0.81 (0.83)	2.17 (2.14)	0.25 (0.24)	0.009 (0.005)	0.0007 (0.0007)	0.006
0.269	0.217	0.81 (0.81)	2.23 (2.28)	0.26 (0.26)	-0.008 (-0.010)	0.0005 (0.0006)	0.005
0.269	0.340	0.84 (0.84)	2.15 (2.19)	0.24 (0.24)	-0.018 (-0.019)	0.0007 (0.0008)	0.007
0.269	0.507	0.87 (0.87)	2.03 (2.06)	0.22 (0.22)	-0.014 (-0.015)	0.0011 (0.0013)	0.009
0.269	0.743	0.92 (0.92)	1.77 (1.78)	0.18 (0.18)	0.005 (0.003)	0.0036 (0.0041)	0.008
0.303	0.005	0.62 (0.64)	2.48 (2.53)	0.37 (0.37)	0.012 (0.014)	0.0035 (0.0029)	0.007
0.303	0.129	0.83 (0.82)	2.03 (2.11)	0.23 (0.24)	0.012 (0.010)	0.0012 (0.0012)	0.006
0.303	0.217	0.82 (0.82)	2.21 (2.29)	0.25 (0.26)	-0.002 (-0.004)	0.0006 (0.0007)	0.005

TABLE IX. (*Continued*)

z	p_T^2 (GeV/c) ²	$\langle y \rangle$	$\langle Q^2 \rangle$ (GeV/c) ²	$\langle x \rangle$	$\mathcal{H}_3/(\mathcal{H}_2 + \epsilon\mathcal{H}_1)$	stat. uncertainty	sys. uncertainty
0.303	0.340	0.83 (0.84)	2.16 (2.20)	0.24 (0.25)	-0.015 (- 0.016)	0.0007 (0.0008)	0.005
0.303	0.507	0.87 (0.87)	2.03 (2.05)	0.22 (0.22)	-0.021 (- 0.022)	0.0011 (0.0013)	0.008
0.303	0.743	0.92 (0.92)	1.86 (1.86)	0.19 (0.19)	0.003 (0.000)	0.0029 (0.0033)	0.009
0.338	0.005	0.63 (0.64)	2.50 (2.53)	0.37 (0.36)	0.016 (0.015)	0.0033 (0.0029)	0.007
0.338	0.026	0.63 (0.62)	2.71 (2.68)	0.40 (0.40)	0.002 (- 0.009)	0.0386 (0.0138)	0.006
0.338	0.129	0.92 (0.92)	1.74 (1.74)	0.18 (0.18)	0.000 (- 0.003)	0.0053 (0.0049)	0.006
0.338	0.217	0.83 (0.83)	2.20 (2.29)	0.25 (0.26)	0.003 (0.000)	0.0008 (0.0009)	0.006
0.338	0.340	0.83 (0.83)	2.16 (2.20)	0.24 (0.25)	-0.011 (- 0.013)	0.0008 (0.0009)	0.006
0.338	0.507	0.86 (0.87)	2.03 (2.06)	0.22 (0.22)	-0.019 (- 0.020)	0.0012 (0.0014)	0.007
0.338	0.743	0.92 (0.92)	1.87 (1.87)	0.19 (0.19)	-0.008 (- 0.011)	0.0030 (0.0034)	0.010
0.375	0.005	0.63 (0.64)	2.50 (2.53)	0.37 (0.36)	0.006 (0.002)	0.0032 (0.0029)	0.007
0.375	0.026	0.67 (0.67)	3.13 (3.11)	0.43 (0.43)	0.018 (- 0.010)	0.0260 (0.0113)	0.004
0.375	0.217	0.84 (0.83)	2.10 (2.19)	0.23 (0.25)	0.003 (0.001)	0.0012 (0.0012)	0.006
0.375	0.340	0.84 (0.84)	2.13 (2.19)	0.24 (0.24)	-0.007 (- 0.010)	0.0010 (0.0011)	0.005
0.375	0.507	0.86 (0.86)	2.04 (2.07)	0.22 (0.22)	-0.015 (- 0.018)	0.0013 (0.0015)	0.005
0.375	0.743	0.92 (0.92)	1.84 (1.88)	0.19 (0.19)	-0.011 (- 0.014)	0.0031 (0.0035)	0.007
0.413	0.005	0.66 (0.68)	2.34 (2.38)	0.33 (0.32)	-0.011 (- 0.011)	0.0051 (0.0044)	0.006
0.413	0.026	0.65 (0.65)	2.37 (2.37)	0.34 (0.34)	-0.003 (- 0.002)	0.1008 (0.0280)	0.007
0.413	0.217	0.87 (0.86)	1.95 (1.99)	0.21 (0.22)	0.001 (- 0.003)	0.0023 (0.0023)	0.004
0.413	0.340	0.86 (0.86)	2.17 (2.24)	0.23 (0.24)	-0.005 (- 0.007)	0.0012 (0.0014)	0.007
0.413	0.507	0.86 (0.87)	2.04 (2.08)	0.22 (0.22)	-0.011 (- 0.013)	0.0015 (0.0017)	0.007
0.413	0.743	0.92 (0.92)	1.85 (1.87)	0.19 (0.19)	-0.016 (- 0.017)	0.0032 (0.0036)	0.004
0.454	0.005	0.66 (0.68)	2.35 (2.37)	0.33 (0.32)	0.000 (- 0.006)	0.0050 (0.0045)	0.007
0.454	0.026	0.68 (0.68)	2.61 (2.59)	0.35 (0.35)	-0.007 (0.004)	0.0401 (0.0141)	0.004
0.454	0.340	0.87 (0.87)	2.02 (2.09)	0.22 (0.22)	-0.010 (- 0.012)	0.0016 (0.0018)	0.005
0.454	0.507	0.89 (0.89)	1.98 (2.02)	0.21 (0.21)	-0.013 (- 0.016)	0.0020 (0.0023)	0.004
0.454	0.743	0.92 (0.92)	1.85 (1.87)	0.19 (0.19)	-0.018 (- 0.024)	0.0035 (0.0041)	0.005
0.496	0.005	0.72 (0.72)	2.63 (2.53)	0.34 (0.32)	0.008 (- 0.010)	0.0080 (0.0068)	0.004
0.496	0.340	0.87 (0.86)	1.96 (2.00)	0.21 (0.22)	-0.011 (- 0.011)	0.0024 (0.0026)	0.007
0.496	0.507	0.92 (0.92)	1.86 (1.88)	0.19 (0.19)	-0.014 (- 0.017)	0.0026 (0.0030)	0.004
0.496	0.743	0.93 (0.92)	1.67 (1.68)	0.17 (0.17)	-0.011 (- 0.014)	0.0051 (0.0061)	0.005
0.540	0.005	0.71 (0.72)	2.19 (2.20)	0.28 (0.28)	0.014 (0.011)	0.0117 (0.0090)	0.005
0.540	0.507	0.92 (0.92)	1.88 (1.91)	0.19 (0.19)	-0.021 (- 0.024)	0.0029 (0.0034)	0.004
0.540	0.743	0.94 (0.94)	1.49 (1.49)	0.15 (0.15)	-0.019 (- 0.042)	0.0102 (0.0120)	0.004
0.586	0.507	0.92 (0.92)	1.74 (1.74)	0.18 (0.18)	-0.016 (- 0.018)	0.0065 (0.0072)	0.005

TABLE X. The extracted data on $\mathcal{H}_4/(\mathcal{H}_2 + \epsilon\mathcal{H}_1)$ averaged over x and Q^2 with their statistical and systematic uncertainties. The values given in brackets are obtained using the fit method.

z	p_T^2 (GeV/c) ²	$\langle y \rangle$	$\langle Q^2 \rangle$ (GeV/c) ²	$\langle x \rangle$	$\mathcal{H}_4/(\mathcal{H}_2 + \epsilon\mathcal{H}_1)$	stat. uncertainty	sys. uncertainty
0.068	0.026	0.84 (0.84)	2.19 (2.26)	0.24 (0.25)	0.001 (0.004)	0.0017 (0.0021)	0.018
0.068	0.065	0.85 (0.85)	2.15 (2.19)	0.24 (0.24)	0.037 (0.028)	0.0013 (0.0018)	0.011
0.093	0.026	0.80 (0.79)	2.23 (2.34)	0.26 (0.28)	0.006 (0.010)	0.0011 (0.0012)	0.013
0.093	0.065	0.80 (0.80)	2.29 (2.32)	0.27 (0.27)	0.012 (0.009)	0.0007 (0.0009)	0.015
0.093	0.129	0.85 (0.85)	2.11 (2.13)	0.23 (0.23)	0.041 (0.032)	0.0013 (0.0016)	0.014
0.093	0.217	0.92 (0.92)	1.86 (1.87)	0.19 (0.19)	0.025 (0.027)	0.0066 (0.0076)	0.007
0.119	0.026	0.79 (0.78)	2.18 (2.27)	0.26 (0.27)	0.009 (0.014)	0.0016 (0.0017)	0.013
0.119	0.065	0.77 (0.77)	2.31 (2.35)	0.28 (0.29)	0.005 (0.004)	0.0008 (0.0009)	0.013
0.119	0.129	0.81 (0.81)	2.24 (2.26)	0.26 (0.26)	0.028 (0.019)	0.0010 (0.0012)	0.014
0.119	0.217	0.85 (0.85)	2.01 (2.02)	0.22 (0.22)	0.051 (0.040)	0.0020 (0.0024)	0.014
0.119	0.340	0.92 (0.92)	1.68 (1.68)	0.17 (0.17)	0.048 (0.051)	0.0142 (0.0157)	0.008
0.147	0.005	0.61 (0.59)	2.75 (2.62)	0.42 (0.41)	0.024 (- 0.034)	0.0279 (0.0166)	0.031
0.147	0.026	0.87 (0.88)	1.85 (1.90)	0.20 (0.20)	0.023 (0.027)	0.0064 (0.0051)	0.016
0.147	0.065	0.75 (0.75)	2.29 (2.34)	0.29 (0.29)	0.009 (0.010)	0.0009 (0.0011)	0.014
0.147	0.129	0.78 (0.78)	2.25 (2.28)	0.27 (0.27)	0.008 (0.005)	0.0010 (0.0012)	0.012
0.147	0.217	0.82 (0.84)	2.14 (2.43)	0.24 (0.27)	0.029 (0.023)	0.0015 (0.0015)	0.014
0.147	0.340	0.91 (0.91)	1.97 (1.99)	0.20 (0.20)	0.068 (0.060)	0.0048 (0.0054)	0.020
0.175	0.005	0.59 (0.61)	2.53 (2.60)	0.39 (0.39)	-0.008 (- 0.011)	0.0126 (0.0100)	0.024
0.175	0.065	0.77 (0.76)	2.26 (2.33)	0.28 (0.29)	0.003 (0.004)	0.0011 (0.0013)	0.013

TABLE X. (Continued)

z	p_T^2 (GeV/c) ²	$\langle y \rangle$	$\langle Q^2 \rangle$ (GeV/c) ²	$\langle x \rangle$	$\mathcal{H}_4/(\mathcal{H}_2 + \epsilon\mathcal{H}_1)$	stat. uncertainty	sys. uncertainty
0.175	0.129	0.78 (0.78)	2.32 (2.35)	0.28 (0.28)	-0.004 (-0.006)	0.0010 (0.0012)	0.015
0.175	0.217	0.81 (0.80)	2.21 (2.23)	0.26 (0.26)	0.010 (0.007)	0.0014 (0.0016)	0.014
0.175	0.340	0.85 (0.85)	2.02 (2.03)	0.22 (0.22)	0.060 (0.049)	0.0027 (0.0030)	0.014
0.175	0.507	0.92 (0.92)	1.85 (1.86)	0.19 (0.19)	0.068 (0.062)	0.0105 (0.0115)	0.030
0.205	0.005	0.61 (0.63)	2.67 (2.71)	0.40 (0.40)	0.017 (0.018)	0.0083 (0.0072)	0.022
0.205	0.065	0.77 (0.76)	2.17 (2.25)	0.26 (0.28)	0.010 (0.012)	0.0015 (0.0017)	0.011
0.205	0.129	0.77 (0.77)	2.32 (2.35)	0.28 (0.29)	-0.008 (-0.011)	0.0011 (0.0013)	0.013
0.205	0.217	0.80 (0.80)	2.26 (2.28)	0.26 (0.27)	-0.007 (-0.010)	0.0014 (0.0017)	0.015
0.205	0.340	0.84 (0.84)	2.15 (2.17)	0.24 (0.24)	0.034 (0.031)	0.0024 (0.0027)	0.015
0.205	0.507	0.92 (0.92)	1.86 (1.87)	0.19 (0.19)	0.099 (0.084)	0.0079 (0.0088)	0.025
0.236	0.005	0.61 (0.62)	2.60 (2.62)	0.39 (0.39)	0.009 (-0.001)	0.0063 (0.0060)	0.023
0.236	0.065	0.84 (0.83)	1.87 (1.88)	0.21 (0.21)	0.006 (0.010)	0.0044 (0.0044)	0.009
0.236	0.129	0.77 (0.77)	2.31 (2.35)	0.28 (0.29)	0.001 (-0.002)	0.0012 (0.0015)	0.011
0.236	0.217	0.78 (0.78)	2.26 (2.28)	0.27 (0.27)	-0.008 (-0.011)	0.0014 (0.0017)	0.014
0.236	0.340	0.81 (0.81)	2.15 (2.16)	0.25 (0.25)	0.005 (0.007)	0.0021 (0.0024)	0.014
0.236	0.507	0.87 (0.87)	1.93 (1.93)	0.20 (0.21)	0.084 (0.078)	0.0053 (0.0060)	0.020
0.236	0.743	0.92 (0.92)	1.67 (1.68)	0.17 (0.17)	0.070 (0.074)	0.0226 (0.0252)	0.034
0.269	0.005	0.63 (0.64)	2.66 (2.67)	0.39 (0.38)	0.007 (0.002)	0.0063 (0.0062)	0.022
0.269	0.129	0.77 (0.77)	2.23 (2.29)	0.27 (0.28)	0.011 (0.008)	0.0015 (0.0018)	0.012
0.269	0.217	0.78 (0.78)	2.26 (2.29)	0.27 (0.27)	-0.009 (-0.012)	0.0015 (0.0018)	0.013
0.269	0.340	0.81 (0.81)	2.16 (2.17)	0.25 (0.25)	0.007 (0.007)	0.0021 (0.0024)	0.013
0.269	0.507	0.84 (0.84)	2.02 (2.03)	0.22 (0.22)	0.047 (0.042)	0.0039 (0.0045)	0.020
0.269	0.743	0.92 (0.92)	1.79 (1.80)	0.18 (0.18)	0.088 (0.072)	0.0162 (0.0179)	0.021
0.303	0.005	0.63 (0.64)	2.51 (2.52)	0.36 (0.36)	0.013 (0.011)	0.0069 (0.0069)	0.021
0.303	0.129	0.79 (0.78)	2.06 (2.11)	0.25 (0.25)	0.010 (0.008)	0.0023 (0.0026)	0.010
0.303	0.217	0.79 (0.79)	2.27 (2.30)	0.27 (0.27)	-0.004 (-0.007)	0.0017 (0.0021)	0.013
0.303	0.340	0.80 (0.80)	2.17 (2.19)	0.25 (0.25)	0.005 (0.006)	0.0022 (0.0025)	0.013
0.303	0.507	0.84 (0.84)	2.02 (2.03)	0.22 (0.22)	0.034 (0.032)	0.0039 (0.0044)	0.022
0.303	0.743	0.92 (0.92)	1.86 (1.86)	0.19 (0.19)	0.103 (0.094)	0.0127 (0.0144)	0.028
0.338	0.005	0.64 (0.65)	2.50 (2.51)	0.36 (0.36)	-0.001 (-0.001)	0.0067 (0.0069)	0.021
0.338	0.026	0.62 (0.62)	2.66 (2.64)	0.39 (0.39)	-0.026 (-0.032)	0.0351 (0.0203)	0.022
0.338	0.129	0.92 (0.92)	1.74 (1.74)	0.18 (0.18)	0.001 (-0.004)	0.0120 (0.0135)	0.007
0.338	0.217	0.79 (0.79)	2.26 (2.31)	0.27 (0.27)	0.001 (-0.001)	0.0020 (0.0024)	0.010
0.338	0.340	0.80 (0.80)	2.17 (2.19)	0.25 (0.26)	0.005 (0.002)	0.0023 (0.0028)	0.010
0.338	0.507	0.84 (0.84)	2.02 (2.04)	0.22 (0.23)	0.020 (0.017)	0.0039 (0.0046)	0.010
0.338	0.743	0.92 (0.92)	1.86 (1.86)	0.19 (0.19)	0.087 (0.088)	0.0124 (0.0138)	0.015
0.375	0.005	0.64 (0.65)	2.49 (2.49)	0.36 (0.36)	-0.007 (-0.007)	0.0069 (0.0073)	0.020
0.375	0.026	0.67 (0.67)	3.11 (3.11)	0.43 (0.43)	-0.004 (-0.036)	0.0271 (0.0198)	0.018
0.375	0.217	0.80 (0.80)	2.14 (2.20)	0.25 (0.26)	-0.004 (-0.005)	0.0026 (0.0031)	0.010
0.375	0.340	0.81 (0.81)	2.14 (2.17)	0.25 (0.25)	0.000 (-0.006)	0.0027 (0.0033)	0.009
0.375	0.507	0.84 (0.84)	2.04 (2.05)	0.23 (0.23)	0.013 (0.007)	0.0042 (0.0049)	0.009
0.375	0.743	0.92 (0.92)	1.86 (1.87)	0.19 (0.19)	0.067 (0.066)	0.0124 (0.0143)	0.010
0.413	0.005	0.67 (0.68)	2.34 (2.37)	0.32 (0.32)	-0.018 (-0.024)	0.0105 (0.0106)	0.015
0.413	0.026	0.65 (0.65)	2.37 (2.37)	0.34 (0.34)	-0.020 (-0.018)	0.0851 (0.0357)	0.018
0.413	0.217	0.84 (0.83)	1.97 (1.99)	0.22 (0.22)	0.002 (-0.006)	0.0048 (0.0054)	0.013
0.413	0.340	0.84 (0.83)	2.20 (2.24)	0.24 (0.25)	0.005 (-0.001)	0.0033 (0.0040)	0.010
0.413	0.507	0.84 (0.84)	2.03 (2.05)	0.22 (0.23)	0.003 (-0.003)	0.0046 (0.0054)	0.016
0.413	0.743	0.92 (0.92)	1.86 (1.88)	0.19 (0.19)	0.037 (0.036)	0.0132 (0.0153)	0.014
0.454	0.005	0.68 (0.68)	2.36 (2.36)	0.32 (0.32)	0.024 (0.011)	0.0104 (0.0108)	0.014
0.454	0.026	0.67 (0.68)	2.56 (2.58)	0.35 (0.35)	-0.053 (-0.031)	0.0392 (0.0226)	0.015
0.454	0.340	0.84 (0.84)	2.03 (2.06)	0.23 (0.23)	0.000 (-0.002)	0.0041 (0.0050)	0.017
0.454	0.507	0.87 (0.87)	1.95 (1.97)	0.21 (0.21)	0.005 (-0.002)	0.0064 (0.0078)	0.009
0.454	0.743	0.92 (0.92)	1.86 (1.87)	0.19 (0.19)	0.036 (0.016)	0.0143 (0.0168)	0.019
0.496	0.005	0.72 (0.72)	2.50 (2.49)	0.32 (0.32)	-0.017 (-0.037)	0.0160 (0.0165)	0.012
0.496	0.340	0.83 (0.83)	1.98 (2.01)	0.22 (0.22)	0.006 (0.009)	0.0055 (0.0066)	0.018
0.496	0.507	0.90 (0.91)	1.83 (1.85)	0.19 (0.19)	-0.008 (-0.007)	0.0092 (0.0116)	0.010
0.496	0.743	0.92 (0.92)	1.68 (1.68)	0.17 (0.17)	-0.014 (-0.005)	0.0201 (0.0245)	0.009
0.540	0.005	0.71 (0.72)	2.18 (2.20)	0.28 (0.28)	0.009 (0.005)	0.0201 (0.0209)	0.010
0.540	0.507	0.92 (0.92)	1.89 (1.90)	0.19 (0.19)	-0.006 (-0.005)	0.0108 (0.0137)	0.016
0.540	0.743	0.94 (0.94)	1.49 (1.49)	0.15 (0.15)	-0.006 (-0.081)	0.0444 (0.0569)	0.022
0.586	0.507	0.92 (0.92)	1.74 (1.74)	0.18 (0.18)	-0.013 (-0.010)	0.0195 (0.0250)	0.016

National Science Foundation, an Emmy Noether grant from the Deutsche Forschungsgemeinschaft and the Korean Science and Engineering Foundation. Jefferson Science Associates (JSA) operates the Thomas Jefferson

National Accelerator Facility for the United States Department of Energy under Contract No. DE-AC05-84ER40150.

-
- [1] L. Trentadue and G. Veneziano, *Phys. Lett. B* **323**, 201 (1994).
- [2] X. Ji, J. P. Ma, and F. Yuan, *Phys. Rev. D* **71**, 034005 (2005).
- [3] M. Grazzini, *Nucl. Phys.* **B518**, 303 (1998).
- [4] J. C. Collins, *Phys. Rev. D* **57**, 3051 (1998).
- [5] X. Ji, J. P. Ma, and F. Yuan, *Phys. Lett. B* **597**, 299 (2004).
- [6] J. Ashman *et al.*, *Z. Phys. C* **52**, 361 (1991).
- [7] M. R. Adams *et al.*, *Z. Phys. C* **76**, 441 (1997).
- [8] F. D. Aaron *et al.*, *Phys. Lett. B* **654**, 148 (2007).
- [9] J. Breitweg *et al.*, *Eur. Phys. J. C* **11**, 251 (1999).
- [10] A. Airapetian *et al.*, *Eur. Phys. J. C* **21**, 599 (2001).
- [11] J. T. Dakin *et al.*, *Phys. Rev. Lett.* **31**, 786 (1973).
- [12] C. J. Bebek *et al.*, *Phys. Rev. D* **15**, 3085 (1977).
- [13] C. J. Bebek *et al.*, *Phys. Rev. D* **16**, 1986 (1977).
- [14] A. Browman *et al.*, *Phys. Rev. Lett.* **37**, 651 (1976).
- [15] T. Navasardyan *et al.*, *Phys. Rev. Lett.* **98**, 022001 (2007).
- [16] H. Mkrtchyan *et al.*, *Phys. Lett. B* **665**, 20 (2008).
- [17] A. Bacchetta, U. D'Alesio, M. Diehl, and C. A. Miller, *Phys. Rev. D* **70**, 117504 (2004).
- [18] J. Levelt and P. J. Mulders, *Phys. Rev. D* **49**, 96 (1994).
- [19] D. Boer and P. J. Mulders, *Phys. Rev. D* **57**, 5780 (1998).
- [20] R. Ent and H. Mkrtchyan, Report No. PR12-06-104, 2006, http://www.jlab.org/exp_prog/PACpage/pac.html.
- [21] C. J. Bebek *et al.*, *Phys. Rev. Lett.* **38**, 1051 (1977).
- [22] J. Chay, S. D. Ellis, and W. J. Stirling, *Phys. Rev. D* **45**, 46 (1992).
- [23] H. L. Lai *et al.*, *Eur. Phys. J. C* **12**, 375 (2000).
- [24] M. Gluck, E. Reya, and A. Vogt, *Z. Phys. C* **67**, 433 (1995).
- [25] A. D. Martin, R. G. Roberts, W. J. Stirling, and R. S. Thorne, *Eur. Phys. J. C* **4**, 463 (1998).
- [26] S. Kretzer, *Phys. Rev. D* **62**, 054001 (2000).
- [27] B. A. Kniehl, G. Kramer, and B. Potter, *Nucl. Phys.* **B582**, 514 (2000).
- [28] S. Albino, B. A. Kniehl, and G. Kramer, *Nucl. Phys.* **B725**, 181 (2005).
- [29] S. Chekanov *et al.*, *Nucl. Phys.* **B658**, 3 (2003).
- [30] S. Chekanov *et al.*, *Nucl. Phys.* **B776**, 1 (2007).
- [31] R. N. Cahn, *Phys. Rev. D* **40**, 3107 (1989).
- [32] M. Anselmino *et al.*, *Phys. Rev. D* **71**, 074006 (2005).
- [33] M. Anselmino *et al.*, *Eur. Phys. J. A* **31**, 373 (2007).
- [34] V. Barone, A. Prokudin, and B. Q. Ma, *Phys. Rev. D* **78**, 045022 (2008).
- [35] E. Berger, *Z. Phys. C* **4**, 289 (1980).
- [36] B. Zhang, Z. Lu, B. Q. Ma, and I. Schmidt, *Phys. Rev. D* **78**, 034035 (2008).
- [37] K. A. Oganessian *et al.*, *Eur. Phys. J. C* **5**, 681 (1998).
- [38] L. P. Gamberg, G. R. Goldstein, and K. A. Oganessian, *Phys. Rev. D* **67**, 071504(R) (2003).
- [39] L. P. Gamberg, G. R. Goldstein, and K. A. Oganessian, *Phys. Rev. D* **68**, 051501(R) (2003).
- [40] E. Di Salvo (private communication).
- [41] A. Brandenburg, V. V. Khoze, and D. Mueller, *Phys. Lett. B* **347**, 413 (1995).
- [42] J. C. Collins, *Nucl. Phys.* **B396**, 161 (1993).
- [43] M. Anselmino *et al.*, *Phys. Rev. D* **75**, 054032 (2007).
- [44] B. Mecking *et al.*, *Nucl. Instrum. Methods Phys. Res., Sect. A* **503**, 513 (2003).
- [45] M. D. Mestayer *et al.*, *Nucl. Instrum. Methods Phys. Res., Sect. A* **449**, 81 (2000).
- [46] E. S. Smith *et al.*, *Nucl. Instrum. Methods Phys. Res., Sect. A* **432**, 265 (1999).
- [47] G. Adams *et al.*, *Nucl. Instrum. Methods Phys. Res., Sect. A* **465**, 414 (2001).
- [48] M. Amarian *et al.*, *Nucl. Instrum. Methods Phys. Res., Sect. A* **460**, 239 (2001).
- [49] K. Park *et al.*, *Phys. Rev. C* **77**, 015208 (2008).
- [50] M. Osipenko *et al.*, *Phys. Rev. C* **73**, 045205 (2006).
- [51] CLAS GEANT simulation, http://improv.unh.edu/Maurik/gsim_info.shtml.
- [52] I. Akushevich, A. Ilyichev, and M. Osipenko, *Phys. Lett. B* **672**, 35 (2009).
- [53] D. Drechsel, S. S. Kamalov, and L. Tiator, *Nucl. Phys.* **A645**, 145 (1999).
- [54] A. Browman *et al.*, *Phys. Rev. Lett.* **35**, 1313 (1975).
- [55] J. Arrington, W. Melnitchouk, and J. A. Tjon, *Phys. Rev. C* **76**, 035205 (2007).
- [56] I. Akushevich, N. Shumeiko, and A. Soroko, *Eur. Phys. J. C* **10**, 681 (1999).
- [57] CERN Program Library, <http://wwwinfo.cern.ch/asd/cernlib/overview.html>.
- [58] H. Avakian *et al.*, *Phys. Rev. D* **69**, 112004 (2004).
- [59] M. Mestayer, Report No. CLAS-NOTE-2004-012, 2004, <http://www.jlab.org/Hall-B/notes/>.
- [60] F. A. Ceccopieri and L. Trentadue, *Phys. Lett. B* **660**, 43 (2008).
- [61] W. Furmanski and R. Petronzio, *Z. Phys. C* **11**, 293 (1982).
- [62] G. Ridolfi and S. Forte, *J. Phys. G* **25**, 1555 (1999).
- [63] S. Catani and L. Trentadue, *Nucl. Phys.* **B327**, 323 (1989).
- [64] P. Nadolsky, D. R. Stump, and C. P. Yuan, *Phys. Rev. D* **61**, 014003 (1999).
- [65] D. de Florian, R. Sassot, and M. Stratmann, *Phys. Rev. D* **75**, 114010 (2007).
- [66] D. Graudenz, *Fortschr. Phys.* **45**, 629 (1997).
- [67] J. M. Laget, *Phys. Lett. B* **489**, 313 (2000).
- [68] G. Ingelman and P. E. Schlein, *Phys. Lett. B* **152**, 256 (1985).
- [69] M. Basile *et al.*, *Nuovo Cimento A* **66**, 129 (1981).

- [70] M. Arneodo *et al.*, Phys. Lett. B **150**, 458 (1985).
[71] B. Andersson *et al.*, Phys. Rep. **97**, 31 (1983).
[72] J.J. Aubert *et al.*, Phys. Lett. B **130**, 118 (1983).
[73] A. König and P. Kroll, Z. Phys. C **16**, 89 (1982).
[74] L.P. Gamberg, G.R. Goldstein, and M. Schlegel, Phys. Rev. D **77**, 094016 (2008).
[75] CLAS Reaction database, <http://clasweb.jlab.org/physicsdb/intro.html>.
[76] M. Osipenko *et al.*, arXiv:0809.1153.
[77] M. Osipenko *et al.*, Phys. Rev. D **67**, 092001 (2003).